

All-inorganic perovskite nanocrystal scintillators

Qiushui Chen¹, Jing Wu², Xiangyu Ou^{3,4}, Bolong Huang⁵, Jawaher Almutlaq⁶, Ayan A. Zhumekenov⁶, Xinwei Guan⁶, Sanyang Han¹, Liangliang Liang¹, Zhigao Yi¹, Juan Li^{3,4}, Xiaoji Xie⁷, Yu Wang⁸, Ying Li⁸, Dianyuan Fan⁸, Daniel B. L. Teh⁹, Angelo H. All^{9,10}, Omar F. Mohammed⁶, Osman M. Bakr⁶, Tom Wu¹¹, Marco Bettinelli¹², Huanghao Yang^{3,4*}, Wei Huang^{7,13,14,15*} & Xiaogang Liu^{1,8,16*}

The rising demand for radiation detection materials in many applications has led to extensive research on scintillators^{1–3}. The ability of a scintillator to absorb high-energy (kiloelectronvolt-scale) X-ray photons and convert the absorbed energy into low-energy visible photons is critical for applications in radiation exposure monitoring, security inspection, X-ray astronomy and medical radiography^{4,5}. However, conventional scintillators are generally synthesized by crystallization at a high temperature and their radioluminescence is difficult to tune across the visible spectrum. Here we describe experimental investigations of a series of all-inorganic perovskite nanocrystals comprising caesium and lead atoms and their response to X-ray irradiation. These nanocrystal scintillators exhibit strong X-ray absorption and intense radioluminescence at visible wavelengths. Unlike bulk inorganic scintillators, these perovskite nanomaterials are solution-processable at a relatively low temperature and can generate X-ray-induced emissions that are easily tunable across the visible spectrum by tailoring the anionic component of colloidal precursors during their synthesis. These features allow the fabrication of flexible and highly sensitive X-ray detectors with a detection limit of 13 nanograys per second, which is about 400 times lower than typical medical imaging doses. We show that these colour-tunable perovskite nanocrystal scintillators can provide a convenient visualization tool for X-ray radiography, as the associated image can be directly recorded by standard digital cameras. We also demonstrate their direct integration with commercial flat-panel imagers and their utility in examining electronic circuit boards under low-dose X-ray illumination.

The nature of the atomic constituents of a scintillator plays an important role in the radioluminescence process of the material because X-ray absorption increases exponentially with atomic number⁶. Although a wide range of scintillation materials containing heavy atoms have been characterized in detail for efficient X-ray scintillation, almost all of these materials are bulk crystals and grown by the Czochralski method⁷ at temperatures above 1,700 °C. For bulk-form scintillators, such as PbWO₄ and Bi₄Ge₃O₁₂, a certain distance of exciton migration is typically needed to transport charge carriers for subsequent trapping by luminescence centres⁸. However, excessive exciton migration is detrimental because it can cause either radioluminescence afterglow or low-efficiency X-ray scintillation. In addition, conventional activator-doped scintillators, such as thallium-activated CsI (CsI:Tl) and cerium-activated YAlO₃ (YAlO₃:Ce), cannot produce tunable scintillation because of their fixed transition energies^{9,10}. Despite enormous efforts, the development of scintillating materials that are low-temperature- and solution-processable,

highly sensitive to X-rays and integrable to flexible substrates remains a daunting challenge.

Recently, bulk crystals of organic–inorganic hybrid perovskites have been found to exhibit large X-ray stopping power^{11–14} and the ability of efficiently converting X-ray photons into charge carriers^{15–18}. The direct photon-to-current conversion can be attributed to the heavy Pb atom¹⁹ and large electron–hole diffusion lengths available in organic–inorganic hybrid perovskites^{20–25}. We reason that caesium lead halide perovskite nanocrystals²⁶, which feature heavy constituent elements and tunable electronic bandgaps in the visible range, could be a promising candidate for high-efficiency X-ray scintillation. An appealing aspect of these perovskite nanocrystals is that their unique electronic structures render highly emissive triplet excited states²⁷ and anomalous fast emission rates²⁸. By virtue of the effect of quantum confinement and increased overlap of electron and hole wavefunctions, the spatial distribution of luminescence centres and X-ray-generated excitons can be confined within the Bohr radius of the nanocrystals. Here we report experimental investigations of multicolour X-ray scintillation from a series of all-inorganic perovskite nanocrystals and demonstrate their use for ultrasensitive X-ray sensing and low-dose digital X-ray technology.

In a typical bulk scintillator material, incident X-ray photons can interact with heavy atoms (for example, Pb, Tl or Ce) to produce a large number of hot electrons through the photoelectric effect⁸. These charge carriers are quickly thermalized to form low-energy excitons, which can subsequently be transported to defect centres or activators for radiative luminescence (Extended Data Fig. 1a). We thus predict that high-energy (kiloelectronvolt-scale) X-ray photons can be converted to numerous low-energy visible photons via direct bandgap emissions in lead halide perovskite nanocrystals (Fig. 1a). To validate this hypothesis, we prepared a series of perovskite nanocrystals (CsPbX₃, with X = Cl, Br or I) by controlling the reaction of Cs-oleate with different PbX₂ precursors via a hot-injection solution method²⁹ (Extended Data Fig. 2). Transmission electron micrograph imaging reveals a cubic shape of the as-synthesized nanocrystals, with an average size of 9.6 nm (Fig. 1b). Remarkably, under X-ray beam excitation the perovskite quantum dots (QDs) yield narrow and colour-tunable emissions (Fig. 1c, Extended Data Fig. 3). This unique property allows multicolour, high-efficiency X-ray scintillation to be realized (Fig. 1d, e, Extended Data Table 1). By contrast, the radioluminescence spectrum of conventional bulk scintillators (CsI:Tl, PbWO₄, YAlO₃:Ce and Bi₄Ge₃O₁₂) is almost invariable and exhibits a wide emission peak with a large full-width at half-maximum (Extended Data Fig. 1b). This inherent limitation of conventional scintillators makes it difficult to achieve multicolour visualization of X-ray irradiation.

¹Department of Chemistry, National University of Singapore, Singapore, Singapore. ²School of Science, China University of Geosciences, Beijing, China. ³MOE Key Laboratory for Analytical Science of Food Safety and Biology, Fuzhou University, Fuzhou, China. ⁴State Key Laboratory of Photocatalysis on Energy and Environment, Fuzhou University, Fuzhou, China. ⁵Department of Applied Biology and Chemical Technology, The Hong Kong Polytechnic University, Hong Kong, China. ⁶Division of Physical Sciences and Engineering, King Abdullah University of Science and Technology, Thuwal, Saudi Arabia. ⁷Institute of Advanced Materials, Nanjing Tech University, Nanjing, China. ⁸SZU-NUS Collaborative Innovation Center for Optoelectronic Science and Technology, Shenzhen University, Shenzhen, China. ⁹Singapore Institute for Neurotechnology, National University of Singapore, Singapore, Singapore. ¹⁰Department of Biomedical Engineering, Johns Hopkins School of Medicine, Baltimore, MD, USA. ¹¹School of Materials Science and Engineering, University of New South Wales, Sydney, New South Wales, Australia. ¹²Luminescent Materials Laboratory, DB, University of Verona, Verona, Italy. ¹³Key Laboratory for Organic Electronics and Information Displays, Nanjing University of Posts and Telecommunications, Nanjing, China. ¹⁴Institute of Advanced Materials, Nanjing University of Posts and Telecommunications, Nanjing, China. ¹⁵Shaanxi Institute of Flexible Electronics, Northwestern Polytechnical University, Xi'an, China. ¹⁶Center for Functional Materials, NUS Suzhou Research Institute, Suzhou, Jiangsu, China. *e-mail: hhyang@fzu.edu.cn; iamwhuang@nwpu.edu.cn; chmlx@nus.edu.sg

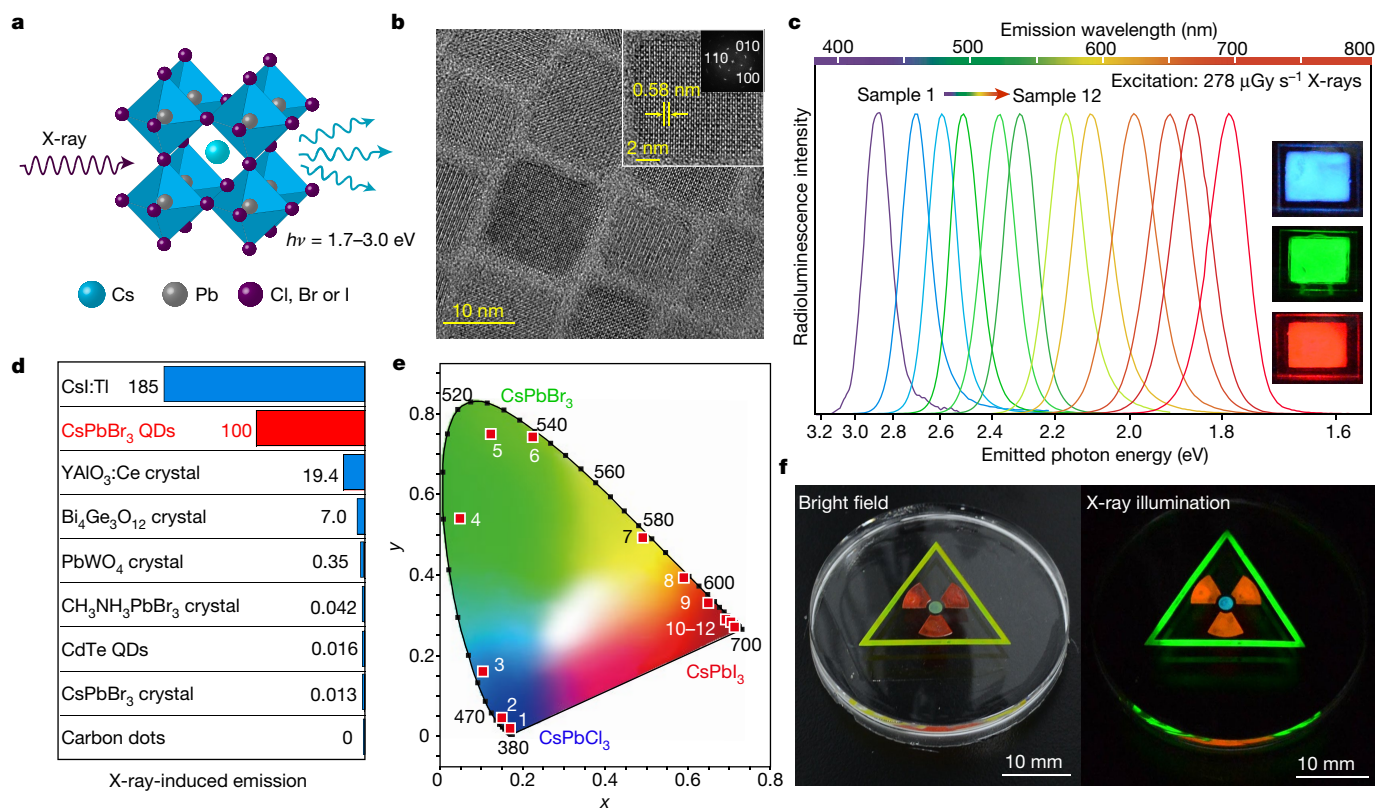


Fig. 1 | Full-colour radioluminescence from perovskite nanocrystal scintillators. **a**, Schematic representation of X-ray-induced luminescence of energy $h\nu$ (where h is the Planck constant and ν is the frequency), generated in an all-inorganic perovskite lattice with a cubic crystal structure (see main text for details). **b**, Low-resolution transmission electron microscopy (TEM) image of the as-synthesized CsPbBr₃ nanocrystals. The inset shows a high-resolution TEM image of a single CsPbBr₃ nanocrystal and the corresponding electron diffraction pattern along the [100] zone axis. **c**, Tunable luminescence spectra of the perovskite QDs under X-ray illumination with a dose rate of $278 \mu\text{Gy s}^{-1}$ at a voltage of 50 kV. The material compositions of samples 1–12 are CsPbCl₃ (1), CsPbCl₂Br (2), CsPbCl_{1.5}Br_{1.5} (3), CsPbClBr₂ (4), CsPbCl₂₋₅Br_{0.5} (5),

CsPbBr₃ (6), CsPbBr₂I (7), CsPbBr_{1.8}I_{1.2} (8), CsPbBr_{1.5}I_{1.5} (9), CsPbBr_{1.2}I_{1.8} (10), CsPbBrI₂ (11) and CsPbI₃ (12). The insets show photographs of the thin-film samples 3, 6 and 9, which emit blue, green and red colours, respectively, upon X-ray irradiation. **d**, Comparison of the optical sensitivity of various scintillator materials in response to exposure to X-rays produced at a voltage of 10 kV. **e**, CIE (Commission Internationale de l'Éclairage) chromaticity coordinates of the X-ray-induced visible emissions measured for samples 1–12. **f**, Multicolour X-ray scintillation (left, bright-field imaging; right, X-ray illumination at a voltage of 50 kV) from three types of perovskite nanocrystal scintillator (orange, CsPbBr₂I; green, CsPbBr₃; blue, CsPbClBr₂).

Inspired by the bandgap-tunable perovskite nanocrystal scintillators, we successfully developed a flexible prototype device for multicolour X-ray scintillation through a combination of solution processing and soft lithography (Fig. 1f, Extended Data Fig. 3d, e). The fabrication of the X-ray-sensing device was made possible by casting the oleate-capped perovskite nanocrystals onto the flexible substrate of interest. This flexible substrate allowed rapid X-ray multicolour visualization (Supplementary Video 1), which is inaccessible by current bulk scintillators.

We then compared the sensitivity of the perovskite nanocrystals to X-ray illumination with that of several of the most widely used commercial bulk scintillators (CsI:Tl, PbWO₄, YAlO₃:Ce and Bi₄Ge₃O₁₂). We used low-dose irradiation of $5.0 \mu\text{Gy s}^{-1}$ (all doses refer to doses in air) at 10 kV and $5 \mu\text{A}$ and found that the ability of CsPbBr₃ nanocrystal thin films (thickness of about 0.1 mm) to convert X-ray photons into visible luminescence is comparable to that of high-efficiency CsI:Tl bulk scintillators (thickness of 5.0 mm), whereas it compares much more favourably (more intense by a factor of 5 or more) than other bulk scintillators, including PbWO₄, YAlO₃:Ce and Bi₄Ge₃O₁₂ (Fig. 1d). This superior performance is attributed to the large X-ray stopping power and high emission quantum yields of the lead halide QDs. Notably, conventional QDs (for example, CdTe QDs and carbon dots) exhibit low-efficiency X-ray-induced luminescence possibly due to weak X-ray absorption³⁰, and thus are not suitable for practical use as scintillators (Fig. 1d, Extended Data Fig. 4). As a point of comparison, we also found

that typical bulk single crystals of CsPbBr₃ and CH₃NH₃PbBr₃ do not exhibit noticeable visible emission under the same experimental conditions (Fig. 1d, Extended Data Fig. 5). The noteworthy scintillation performance of CsPbBr₃ nanocrystals with respect to their bulk counterparts presents a compelling case for investigating the origins of the scintillation process in our system. This process can be explained in part by the lack of exciton confinement in the bulk form, in which discrete or quantized energy levels that give access to visible emission cannot be generated³¹.

We further investigated experimentally and theoretically the physical processes that govern the interaction between X-rays and perovskite nanocrystals. As shown in Fig. 2a, we compared the absorption coefficient of the CsPbBr₃ nanocrystals (highest atomic number $Z_{\text{max}} = 82$; $K\alpha = 88.0 \text{ keV}$) as a function of X-ray photon energy with two types of conventional QD (CdTe, $Z_{\text{max}} = 52$, $K\alpha = 31.8 \text{ keV}$; carbon, $Z_{\text{max}} = 6$, $K\alpha = 0.285 \text{ keV}$). The nature of heavy atomic constituents is critically important for efficient X-ray scintillation, because X-ray absorption scales with the effective atomic number, Z_{eff} as Z_{eff}^4/AE^3 , where A is the atomic mass and E is the X-ray photon energy⁶. We thus speculate that the Pb-based perovskite nanocrystals are much more suitable for efficient X-ray absorption than QDs without the Pb component. We carried out an X-ray photoelectron spectroscopic investigation to record the kinetic process of electrons escaping from the CsPbBr₃ nanocrystal upon irradiation with soft X-rays (Fig. 2b). To reveal the photoionization nature of the X-ray scintillation process under study, we

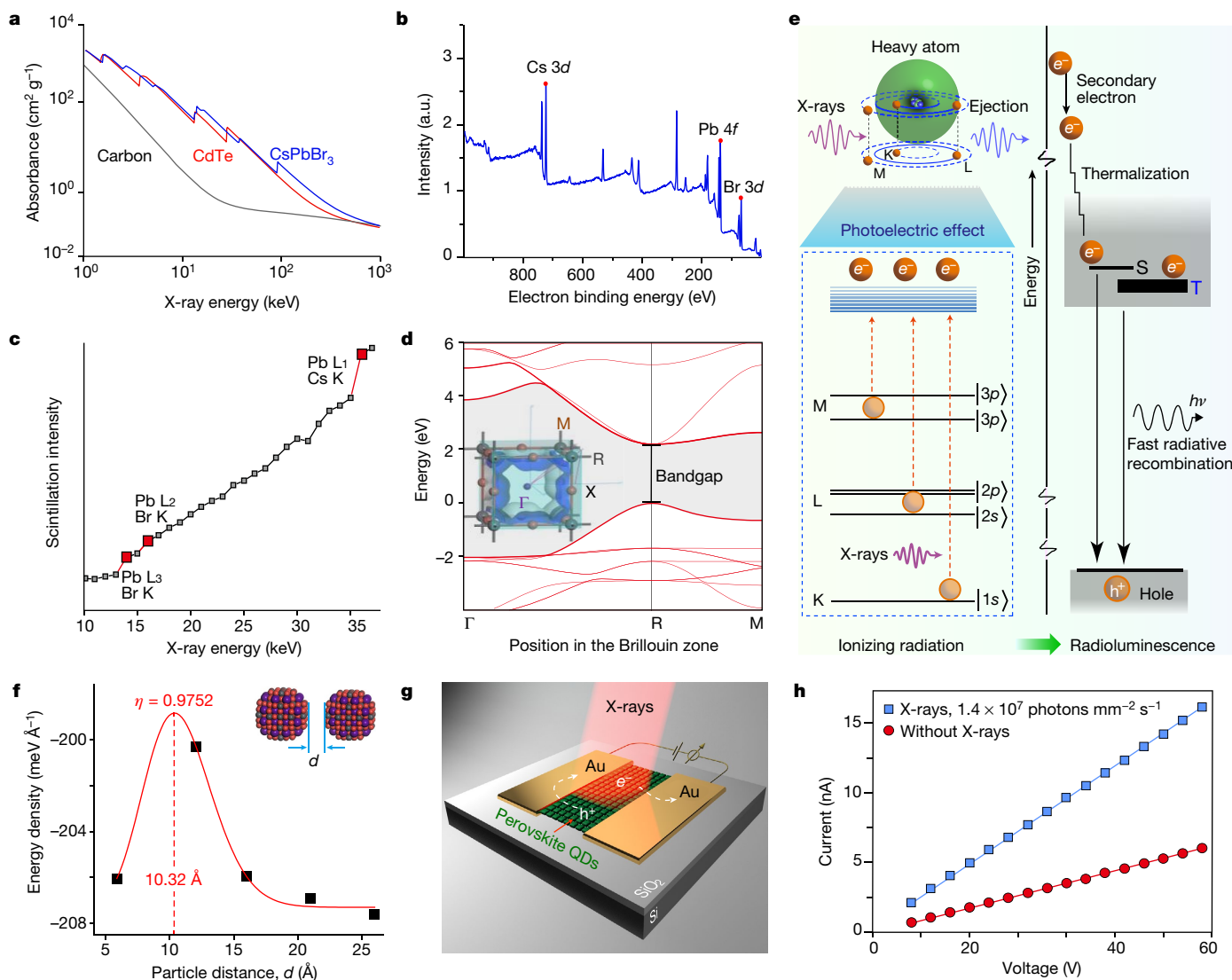


Fig. 2 | Mechanistic investigation of X-ray energy conversion by perovskite nanocrystals. **a**, Measured absorption spectra of CsPbBr₃, CdTe and carbon as a function of X-ray energy. The attenuation coefficients were obtained from ref. ³³. **b**, X-ray photoelectron spectroscopic data of the CsPbBr₃ nanocrystals plotted against the binding energy of the electron. The photoemission peaks Cs 3d, Pb 4f and Br 3d are indicated. a.u., arbitrary units. **c**, Measurement of X-ray-induced luminescence from the perovskite nanocrystals using synchrotron radiation. The electronic edge energies of Pb L, Cs K and Br K (shown as red squares) fall in the X-ray energy range 10–38 keV. The line is a guide for the eye. **d**, Calculated electronic band structures of the CsPbBr₃ nanocrystal. The inset shows the Brillouin zone of the cubic-phased crystal lattice (see Methods for details). **e**, Proposed mechanism of X-ray scintillation in a lead halide perovskite nanocrystal. Upon X-ray irradiation, a high-energy electron (red circles, e⁻) is ejected from a lattice atom through photoelectric ionization (ionizing

radiation creates an energetic electron and a hole in an inner electronic shell). Subsequently, the ejected high-energy electron produces secondary high-energy electrons. The generated hot charge carriers then undergo thermalization and produce low-energy excitons. Next, fast radiative recombination takes place, producing radioluminescence of energy $h\nu$ in either a singlet (S) or triplet (T) state at the electronic band edge. **f**, Energy density on the surface of a CsPbBr₃ cluster as a function of particle distance, d , in the lattice. The red line is a fit with a Gaussian distribution function with a fitting coefficient of $\eta = 0.9752$. The particle distance corresponding to the maximum energy density is 10.32 Å. **g**, Schematic showing the basic design of a perovskite-nanocrystal-based photoconductor used for X-ray sensing. A 10- μm -thick layer of CsPbBr₃ QDs is spin-coated onto the substrate for X-ray photon-carrier conversion. Gold (Au) electrodes are placed onto the QDs for hole-electron extraction. **h**, Current-voltage characteristics of the as-fabricated photoconductor, recorded with and without X-ray illumination.

measured the radioluminescence of the perovskite nanocrystals in response to synchrotron radiation (Fig. 2c, Extended Data Fig. 6, Supplementary Video 2). We observed an abrupt enhancement in the scintillation intensity upon excitation at 14 keV, 16 keV and 36 keV, indicating an X-ray absorption resonance at the electronic edge of the Pb L, Cs K and Br K shells in the CsPbBr₃ structure. Density functional theory calculations confirmed that the electronic band structure of these perovskite nanocrystal scintillators is tunable, which is associated with the tailorability of their valence band through control of the halide composition (Extended Data Fig. 7). The bandgap energy of the perovskite nanocrystal under study is located in the range 1.7–3 eV, suggesting the feasibility of using such a nanomaterial to convert an

absorbed dose of ionizing radiation into visible light (Fig. 2d). In addition, the orbital contour plots of the CsPbBr₃ nanocrystal indicate that the presence of hole-like surface-vacancy-induced Coulomb-trapping states near the Fermi level beyond the valence band maximum is responsible for the electronically energetic confinement of excitons in the perovskite nanocrystal (Extended Data Fig. 8b).

Figure 2e presents a plausible mechanism for the high-intensity radioluminescence from the perovskite nanocrystals. At the initial conversion stage, an incident X-ray photon with energy lower than a few hundred kiloelectronvolts interacts with the lattice atoms of a perovskite nanocrystal, predominantly through the photoelectric effect. During this process a large number of high-energy electrons and holes

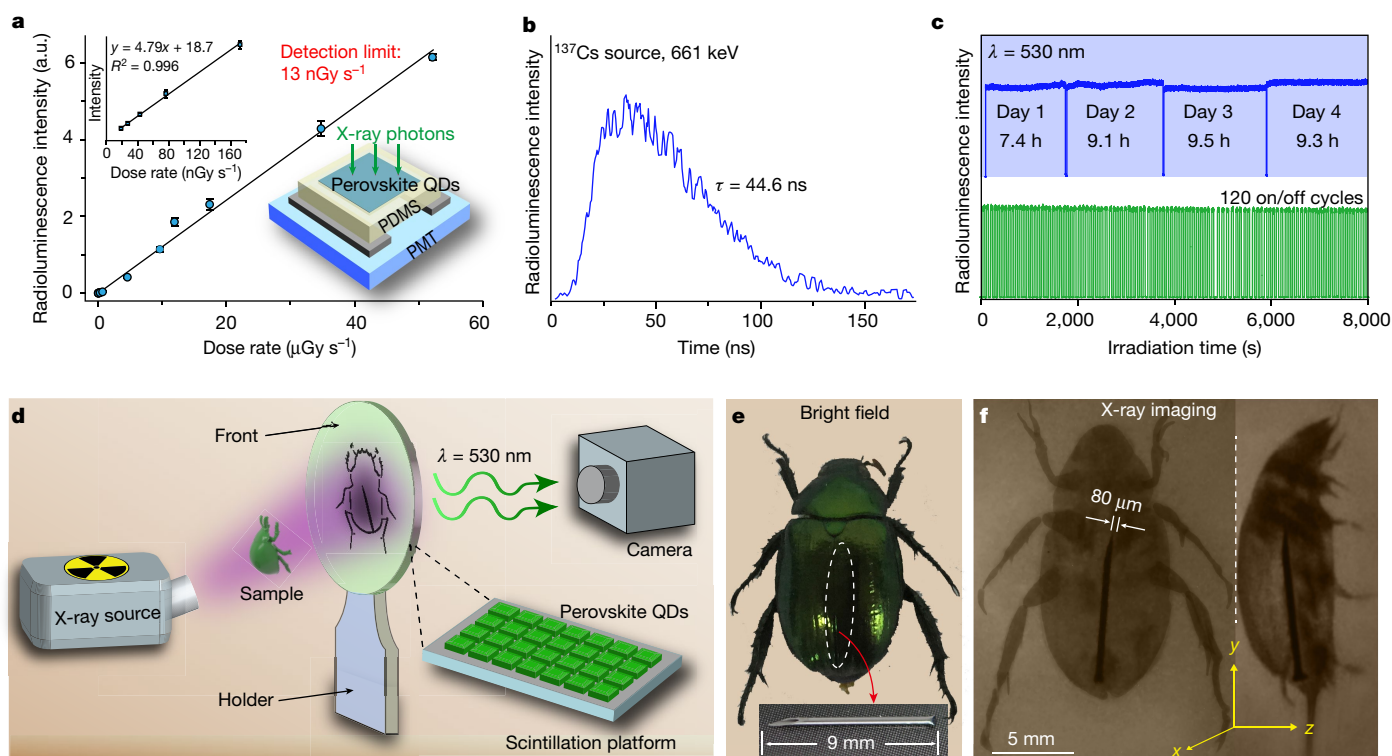


Fig. 3 | Ultrasensitive X-ray sensing and radiography using CsPbBr₃ nanocrystals. **a**, Radioluminescence measurements for a CsPbBr₃-based scintillator as a function of dose rate. The left inset shows radioluminescence profiles measured at low dose rates. The detection limit of 13 nGy s⁻¹ is derived from the slope of the fitting line, with a signal-to-noise ratio of 3. The right inset shows a schematic of the X-ray photodetector, which consists of a CsPbBr₃ nanocrystal thin film (about 120 μm thickness), a polydimethylsiloxane (PDMS) layer and a photomultiplier tube (PMT). All measurements were performed three times. Error bars are mean ± s.d. **b**, Measured radioluminescence decay

of the CsPbBr₃-based scintillator under excitation with a ¹³⁷Cs source (photon energy, 661 keV). The scintillation decay time is $\tau = 44.6$ ns. **c**, Photostability of the CsPbBr₃-based scintillator against continuous X-ray irradiation (wavelength $\lambda = 530$ nm, 50 kV; top) and repeated cycles of X-ray excitation at 30 kV with a time interval of 30 s ($\lambda = 530$ nm; bottom). **d**, Schematic of the experimental setup used for real-time X-ray diagnostic imaging of biological samples. A beetle is placed between the X-ray source and a scintillation platform covered with perovskite QDs. **e**, **f**, Bright-field (**e**) and the X-ray (**f**) images of the sample, recorded with a digital camera. The X-ray images were recorded at a voltage of 50 kV.

can be created, and electronic transport occurs between the perovskite nanocrystals (Fig. 2f). The hot electrons and holes are then quickly thermalized in the conduction and valence band edges. The X-ray-induced charge carriers in the perovskite nanocrystals were experimentally confirmed by measuring the current through a photoconductor upon X-ray illumination (Fig. 2g, h). The trapping and radiative recombination of electron-hole pairs can be controlled to produce a desired luminescence colour by adjusting the bandgap energy. The mechanism of intense X-ray scintillation could be attributed in part to the strong X-ray stopping power and quantum confinement effects of perovskite nanocrystals. Additionally, the scintillation process is dominated by the presence of highly emissive triplet excited states (Fig. 2e), large absorption cross-section within the bandgap (Extended Data Fig. 9a, b) and fast emission output (Extended Data Fig. 9c–e), which are characteristics of perovskite nanocrystals^{27,28,32}.

The solution-processability of the perovskite nanocrystals makes it possible to fabricate a thin-film scintillator device for ultrasensitive X-ray detection. In this device (Fig. 3a), spin-coated CsPbBr₃ nanocrystals are used for X-ray sensing by converting high-energy X-ray photons into visible emission, which is readily detectable by a photomultiplier tube. A favourable characteristic of the prototype X-ray detector is its linear response to the X-ray dose rate, covering a range as broad as four orders of magnitude (Extended Data Fig. 10). The lowest detectable dose rate for X-ray detection is demonstrated to be 13 nGy s⁻¹. This value is about 420 times lower than the dose typically used for X-ray diagnostics (5.5 μGy s⁻¹)¹⁴. This scintillation photodetector also exhibits a very fast response (scintillation decay time, $\tau = 44.6$ ns) upon excitation with pulsed photons (661 keV) from a portable ¹³⁷Cs source (Fig. 3b). The fast response to X-ray photons

is critical to scintillation performance in medical radiography. The photostability of the perovskite nanocrystals was further examined under continuous or repeated cycles of X-ray illumination, as shown in Fig. 3c.

To assess the suitability of the perovskite nanocrystals as scintillators for X-ray phase-contrast imaging, we implanted a metallic needle into a green scarab beetle and imaged the biological specimen with X-rays against a background substrate comprising a thin film of solution-processed CsPbBr₃ nanocrystals (Fig. 3d). We note that the CsPbBr₃ nanocrystals were chosen for this demonstration because their green emission at 530 nm matches well with the maximum wavelength response of a complementary metal-oxide-semiconductor sensor. As shown in Fig. 3e, f, owing to the large difference between the X-ray stopping powers of the needle and the beetle, the needle inside the beetle is clearly revealed by phase-contrast imaging recorded using a common digital camera. The concept of direct X-ray contrast imaging through the use of high-efficiency perovskite nanocrystals is readily applicable to high-throughput electronics inspection and tissue imaging, where common digital cameras can be conveniently used (Extended Data Fig. 11; Extended Data Table 2).

We took a step further and tested the compliance of the perovskite nanocrystals to commercial flat-panel X-ray detectors equipped with α -Si photodiode arrays (Fig. 4a, b). As shown in Fig. 4c, the perovskite-nanocrystal-based X-ray detector shows a modulation transfer function of 0.72 at a spatial resolution of 2.0 line pairs per millimetre, which is much higher than the spatial resolution of commercially used CsI:Tl-based flat-panel X-ray detectors (0.36 at 2.0 line pairs per millimetre). This high spatial resolution could be ascribed to the lower degree of light scattering in the nanoparticle-based thin film

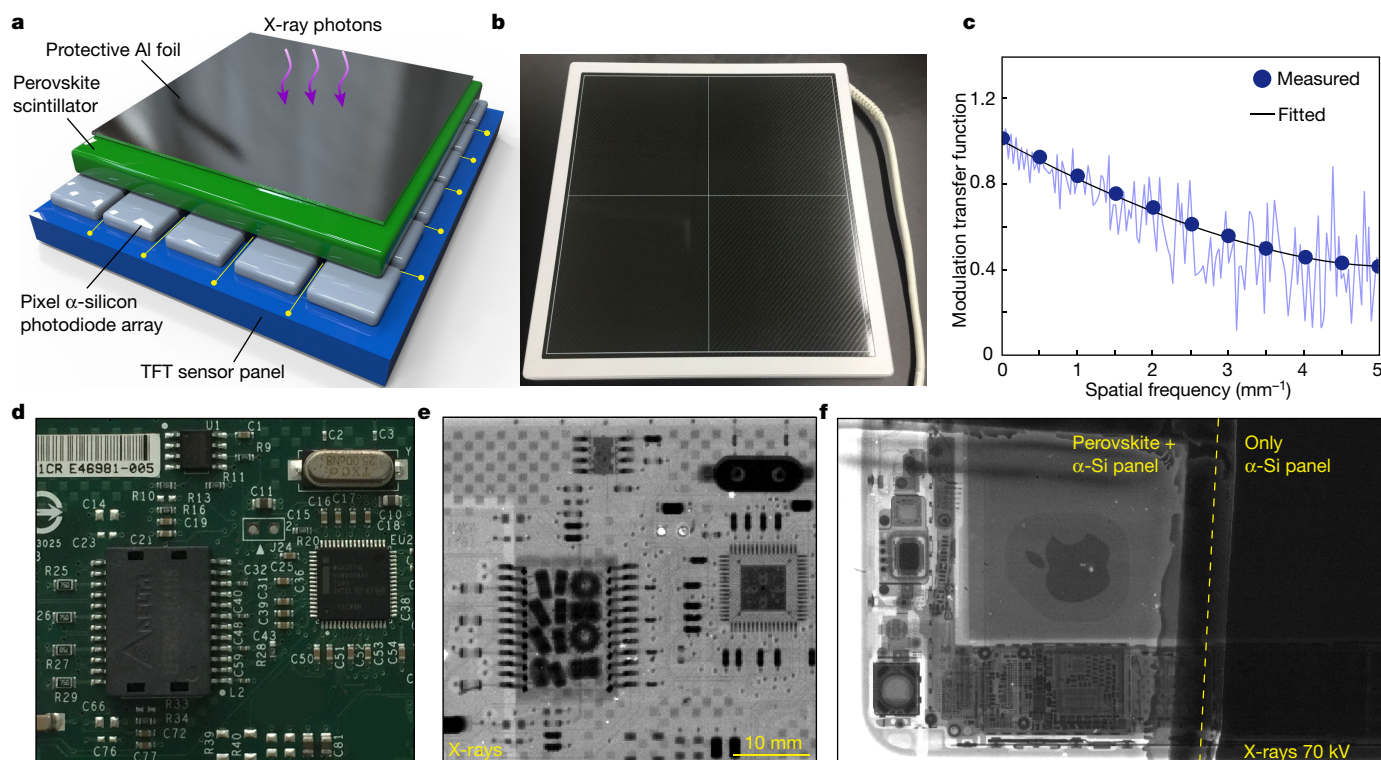


Fig. 4 | Prototype perovskite-nanocrystal-based flat-panel detector for digital radiography. **a**, Multilayered design of the flat-panel X-ray imaging system consisting of a thin-film-transistor (TFT) sensor panel, a pixelated α -silicon photodiode array, a CsPbBr₃ perovskite nanocrystal thin film (about 75 μ m thick) and a protective Al foil cover (40 μ m). **b**, Photograph of the packaged flat-panel detector. **c**, Spatial resolution of the X-ray imaging system, characterized by the modulation transfer

function under 15 μ Gy of X-ray exposure. The blue circles and purple line show measured values and the black line is a fit to the data. **d**, **e**, Digital photograph of a network interface card (**d**) and corresponding X-ray image obtained using the flat-panel detector (70 kV and 2.5 mGy s⁻¹ exposure for 6 ms) (**e**). **f**, Comparison of X-ray images of an Apple iPhone acquired with the perovskite scintillator deposited on an α -Si photodiode panel (left) and only with an α -Si photodiode (right).

compared with that occurring in commercial bulk-scintillator-based films made of thick polycrystalline ceramics or long micropillars. We further used the prototype device to image the internal structures of electronic circuits and an Apple iPhone with a low X-ray dose of 15 μ Gy (Fig. 4d–f). Unlike CsI:Tl scintillators, which have the issue of afterglow luminescence (scintillation decay time of 1,000 ns), our perovskite nanocrystals have a very fast response (44.6 ns) to X-rays, making them ideal for dynamic real-time X-ray imaging.

In conclusion, we have demonstrated inorganic perovskite nanocrystals as a new class of scintillators that are capable of converting small doses of X-ray photons into multicolour visible light. When considering the material's solution-processability and practical scalability, it is envisioned that these scintillators are suitable for the mass production of ultrasensitive X-ray detectors and large-area, flexible X-ray imagers. Compared to conventional CsI:Tl scintillators—whose use is constrained by the risk of thallium poisoning, the presence of afterglow and high-temperature synthesis—perovskite nanocrystals offer several outstanding attributes, including relatively low toxicity, low-temperature solution synthesis, fast scintillation response and high emission quantum yield. Although there is still much to be learned regarding the origin of nanocrystal scintillation, these perovskite nanocrystals may hold substantial promise for advancing X-ray sensing and imaging industry. The thermal and environmental instability issues that are often associated with perovskite materials in photovoltaic and light-emitting-diode applications could be largely avoided through the X-ray scintillation settings.

Online content

Any methods, additional references, Nature Research reporting summaries, source data, statements of data availability and associated accession codes are available at <https://doi.org/10.1038/s41586-018-0451-1>.

Received: 24 October 2017; Accepted: 21 June 2018;
Published online 27 August 2018.

- Röntgen, W. C. On a new kind of rays. *Science* **3**, 227–231 (1896).
- Moretti, F. et al. Radioluminescence sensitization in scintillators and phosphors: trap engineering and modeling. *J. Phys. Chem. C* **118**, 9670–9676 (2014).
- Bücheler, P. et al. X-ray imaging with scintillator-sensitized hybrid organic photodetectors. *Nat. Photon.* **9**, 843–848 (2015).
- Yaffe, M. J. & Rowlands, J. A. X-ray detectors for digital radiography. *Phys. Med. Biol.* **42**, 1–39 (1997).
- Durie, B. G. & Salmon, S. E. Scintillator distribution in high-speed autoradiography. *Science* **190**, 1093–1095 (1975).
- Niki, M. & Yoshikawa, A. Recent R&D trends in inorganic single-crystal scintillator materials for radiation detection. *Adv. Opt. Mater.* **3**, 463–481 (2015).
- Weber, M. J. Inorganic scintillators: today and tomorrow. *J. Lumin.* **100**, 35–45 (2002).
- Rodnyi, P. A. *Physical Processes in Inorganic Scintillators* (CRC Press, Boca Raton, 1997).
- Nagarkar, V. V. et al. Structured CsI(Tl) scintillators for X-ray imaging applications. *IEEE Trans. Nucl. Sci.* **45**, 492–496 (1998).
- Baccaro, S. et al. Scintillation properties of YAP:Ce. *Nucl. Instrum. Methods A* **361**, 209–215 (1995).
- Rowlands, J. A. Material change for X-ray detectors. *Nature* **550**, 47–48 (2017).
- Kim, Y. C. et al. Printable organometallic perovskite enables large-area, low-dose X-ray imaging. *Nature* **550**, 87–91 (2017).
- Wei, W. et al. Monolithic integration of hybrid perovskite single crystals with heterogeneous substrate for highly sensitive X-ray imaging. *Nat. Photon.* **11**, 315–321 (2017).
- Wei, H. et al. Sensitive X-ray detectors made of methylammonium lead tribromide perovskite single crystals. *Nat. Photon.* **10**, 333–339 (2016).
- Yakunin, S. et al. Detection of X-ray photons by solution-processed organic-inorganic perovskites. *Nat. Photon.* **9**, 444–449 (2015).
- Shrestha, S. et al. High-performance direct conversion X-ray detectors based on sintered hybrid lead triiodide perovskite wafers. *Nat. Photon.* **11**, 436–440 (2017).
- Wei, H. et al. Dopant compensation in alloyed CH₃NH₃PbBr_{3-x}Cl_x perovskite single crystals for gamma-ray spectroscopy. *Nat. Mater.* **16**, 826–833 (2017).
- Pan, W. et al. Cs₂AgBiBr₆ single-crystal X-ray detectors with a low detection limit. *Nat. Photon.* **11**, 726–732 (2017).

19. Birowosuto, M. D. et al. X-ray scintillation in lead halide perovskite crystals. *Sci. Rep.* **6**, 37254 (2016).
20. Dong, Q. et al. Electron-hole diffusion lengths $>175\ \mu\text{m}$ in solution-grown $\text{CH}_3\text{NH}_3\text{PbI}_3$ single crystals. *Science* **347**, 967–970 (2015).
21. Shi, D. et al. Low trap-state density and long carrier diffusion in organolead trihalide perovskite single crystals. *Science* **347**, 519–522 (2015).
22. Tan, H. et al. Efficient and stable solution-processed planar perovskite solar cells via contact passivation. *Science* **355**, 722–726 (2017).
23. Li, X. et al. A vacuum flash-assisted solution process for high-efficiency large-area perovskite solar cells. *Science* **353**, 58–62 (2016).
24. Im, J.-H., Jang, I.-H., Pellet, N., Grätzel, M. & Park, N.-G. Growth of $\text{CH}_3\text{NH}_3\text{PbI}_3$ cuboids with controlled size for high-efficiency perovskite solar cells. *Nat. Nanotechnol.* **9**, 927–932 (2014).
25. Son, D.-Y. et al. Self-formed grain boundary healing layer for highly efficient $\text{CH}_3\text{NH}_3\text{PbI}_3$ perovskite solar cells. *Nat. Energy* **1**, 16081 (2016).
26. Protesescu, L. et al. Nanocrystals of cesium lead halide perovskites (CsPbX_3 , $X=\text{Cl}$, Br , and I): novel optoelectronic materials showing bright emission with wide color gamut. *Nano Lett.* **15**, 3692–3696 (2015).
27. Becker, M. A. et al. Bright triplet excitons in caesium lead halide perovskites. *Nature* **553**, 189–193 (2018).
28. Hu, F. et al. Superior optical properties of perovskite nanocrystals as single photon emitters. *ACS Nano* **9**, 12410–12416 (2015).
29. Swarnkar, A. et al. Quantum dot-induced phase stabilization of α - CsPbI_3 perovskite for high-efficiency photovoltaics. *Science* **354**, 92–95 (2016).
30. Hossu, M., Liu, Z., Yao, M., Ma, L. & Chen, W. X-ray luminescence of CdTe quantum dots in $\text{LaF}_3\text{:Ce/CdTe}$ nanocomposites. *Appl. Phys. Lett.* **100**, 013109 (2012).
31. Saidaminov, M. I. et al. Pure Cs_4PbBr_6 : highly luminescent zero-dimensional perovskite solids. *ACS Energy Lett.* **1**, 840–845 (2016).
32. Kovalenko, M. V., Protesescu, L. & Bodnarchuk, M. I. Properties and potential optoelectronic applications of lead halide perovskite nanocrystals. *Science* **358**, 745–750 (2017).
33. Berger, M. J. et al. *XCOM: Photon Cross Sections Database*; <https://www.nist.gov/pml/xcom-photon-cross-sections-database> (2013).

Acknowledgements This work is supported by the King Abdullah University of Science and Technology; the Singapore Ministry of Education (grants R143000627112 and R143000642112); the Agency for Science, Technology and Research (A*STAR) under contracts 122-PSE-0014 and 1231AFG028

(Singapore); the National Research Foundation, Prime Minister's Office, Singapore under its Competitive Research Program (CRP award number NRF-CRP15-2015-03); the National Basic Research Program of China (973 Program, grant number 2015CB932200); the National Natural Science Foundation of China (21635002, 21471109, 21210001 and 21405143); and the Natural Science Foundation of Jiangsu Province (BE2015699). We thank H. Jiang, B. Deng, Z. Fang, Z. Zhou, Y. Zhang, X. Ling, M. Sun and A. Malko for technical assistance.

Reviewer information *Nature* thanks R. Comin, W. Heiss and the other anonymous reviewer(s) for their contribution to the peer review of this work.

Author contributions Q.C. and X.L. conceived and initiated the project. X.L., H.Y. and W.H. supervised the project and led the collaboration efforts. Q.C., X.L., H.Y. and W.H. designed the experiments. Q.C., J.W., L.L. and S.H. performed the nanocrystal synthesis. Q.C., X.O. and J.L. carried out the spectral measurements. Q.C., X.O., Y.W., Y.L., D.F., Z.Y., D.B.L.T. and A.H.L. contributed to the design and implementation of the X-ray sensing experiments. B.H., M.B. and O.F.M. carried out the theoretical calculations. J.A., A.A.Z. and O.M.B. prepared the perovskite single crystals. X.G. and T.W. fabricated the photoconductor devices and performed the photocurrent measurements. X.X. fabricated the PDMS moulds and measured the low-temperature scintillation spectra. Q.C. and X.L. wrote the manuscript. All authors discussed the results and commented on the manuscript.

Competing interests The authors declare no competing interests.

Additional information

Extended data is available for this paper at <https://doi.org/10.1038/s41586-018-0451-1>.

Supplementary information is available for this paper at <https://doi.org/10.1038/s41586-018-0451-1>.

Reprints and permissions information is available at <http://www.nature.com/reprints>.

Correspondence and requests for materials should be addressed to H.Y. or W.H. or X.L.

Publisher's note: Springer Nature remains neutral with regard to jurisdictional claims in published maps and institutional affiliations.

METHODS

Chemicals. Caesium carbonate (Cs_2CO_3 , 99.9%), lead(II) chloride (PbCl_2 , 99.99%), lead(II) bromide (PbBr_2 , 99.99%), lead(II) iodide (PbI_2 , 99.99%), oleylamine (technical grade 70%), oleic acid (technical grade 90%), 1-octadecene (technical grade 90%) and cyclohexane (chromatography grade 99.9%) were purchased from Sigma-Aldrich. Silicon wafers were obtained from Xilika Crystal Polishing Material Co., Ltd (Tianjin, China). SU-8 photoresist (2050) and developer solution were purchased from Microchem Corp. (Newton, MA). A Sylgard 184 silicone elastomer kit was purchased from Dow Corning for the preparation of polydimethylsiloxane (PDMS) substrates. Crystals of CsI:Tl, $\text{Bi}_4\text{Ge}_3\text{O}_{12}$, YAlO_3 :Ce and PbWO_4 scintillators were purchased from Zhonghelixin Co., Ltd (Chengdu, China). CdTe QDs were obtained from Xingzi New Material Technology Development Co., Ltd (Shanghai, China). Unless otherwise noted, all the reagents were used without additional treatment.

Synthesis of Cs-oleate as a caesium precursor. In a typical synthesis procedure, Cs_2CO_3 (0.4 g, 1.23 mmol), oleic acid (1.25 ml) and octadecene (15 ml) were added to a two-neck round-bottom flask (50 ml). The resulting mixture was heated to 100 °C under vigorous stirring and vacuum conditions for 0.5 h. After that, a nitrogen purge and vacuum were alternately applied to the flask three times to remove moisture and O_2 . Subsequently, the mixture was heated to 150 °C and the solution became clear, indicating the completion of the reaction between Cs_2CO_3 and oleic acid. The Cs-precursor solution was kept at 150 °C in a nitrogen atmosphere before the synthesis of perovskite nanocrystal.

Synthesis of CsPbX_3 (X = Cl, Br or I) nanocrystals. The CsPbX_3 perovskite QDs were synthesized by a modified hot-injection procedure²⁹. In a typical experiment, PbX_2 (0.36 mmol each for X = Cl, Br or I), oleic acid (1.0 ml), oleylamine (1.0 ml) and octadecene (10 ml) were added to a two-neck round-bottom flask (50 ml). The resulting mixture was heated to 100 °C under vigorous stirring and vacuum conditions for 0.5 h, at which time the moisture residue was removed by purging with nitrogen and vacuum suction. Then the mixture was heated to 160 °C until the PbX_2 precursors dissolved completely. A hot Cs-oleate precursor solution (1 ml) was injected quickly into the above reaction mixture. After 5 s of reaction, the flask was transferred into an ice bath. The CsPbX_3 QDs were obtained by centrifugation at 13,000 r.p.m. for 10 min and stored in 4 ml of cyclohexane before further use. Mixed-halide perovskite QDs were synthesized to tune the luminescence colour. Samples 1–12 correspond to the as-synthesized CsPbCl_3 (1), CsPbCl_2Br (2), $\text{CsPbCl}_{1.5}\text{Br}_{1.5}$ (3), CsPbClBr_2 (4), $\text{CsPbCl}_{2.5}\text{Br}_{0.5}$ (5), CsPbBr_3 (6), CsPbBr_2I (7), $\text{CsPbBr}_{1.8}\text{I}_{1.2}$ (8), $\text{CsPbBr}_{1.5}\text{I}_{1.5}$ (9), $\text{CsPbBr}_{1.2}\text{I}_{1.8}$ (10), CsPbBrI_2 (11) and CsPbI_3 (12) QDs.

Growth of lead halide perovskite single crystals. The growth of CsPbBr_3 single crystals was carried out according to a method described in the literature³⁴. In a typical procedure, CsBr (0.64 g, 3 mmol) and PbBr_2 (2.2 g, 6 mmol) were dissolved in 3 ml of dimethyl sulfoxide and stirred for 1 h. Subsequently, 1.5 ml of the mixture was transferred into a vial heated at 60 °C, and the temperature was raised to 100 °C with a heating rate of 10 °C h^{-1} . At 100 °C, the solution was filtered and then gradually heated to 120 °C. We observed the growth of small-sized crystals with increasing temperature. The resulting crystals were washed with hot dimethyl sulfoxide and dried in vacuo at 100 °C for 1 h. For the synthesis of $\text{CH}_3\text{NH}_3\text{PbBr}_3$ (MAPbBr_3) single crystals, a mixture of PbBr_2 and $\text{CH}_3\text{NH}_3\text{Br}$ (1.5 mol each) was dissolved in a solution of *N,N*-dimethyl formamide (1 ml) at room temperature. The solution was purified by passing through a polytetrafluoroethylene filter with a pore size of 0.22 μm . The growth of the MAPbBr_3 single crystals was carried out in an oil bath heated at 60 °C and under ambient pressure.

Synthesis of fluorescent carbon dots. Fluorescent carbon dots were synthesized by a hydrothermal method. In a typical experiment, ammonium citrate (0.972 g, 4.0 mmol) was first dissolved in a 20-ml water solution. The solution was then transferred into a 30-ml Teflon-lined vessel at room temperature while stirring. Subsequently, the solution was heated to 190 °C and kept at that temperature for 10 h. After cooling to room temperature, the product was purified using dialysis, and the cut-off molecular weight of the dialysed membrane was equivalent to about 2,000. The carbon dot solution was concentrated using a rotary evaporator.

Preparation of silica-coated perovskite nanocrystals. The stability of perovskite nanocrystals was improved by coating with a silicon dioxide (silica) layer according to the literature³⁵. In a typical procedure, the CsPbBr_3 QDs, dispersed in cyclohexane (2 ml), were introduced into a 50-ml flask containing 10 ml of toluene solution ($\geq 99.5\%$; AnalaR NORMAPUR). 100 μl of tetramethoxysilane was injected quickly into the mixture at room temperature. After stirring for 2 h, the products were isolated through centrifugation at 13,000 r.p.m. for 8 min. The silica-coated CsPbX_3 (X = Br or I) QDs were either dispersed in cyclohexane or dried in air.

Physical characterization. Powder X-ray diffraction characterization was carried out by an ADDS wide-angle X-ray powder diffractometer with $\text{Cu K}\alpha$ radiation (wavelength, $\lambda = 1.54184 \text{ \AA}$). TEM imaging was performed using a FEI Tecnai G20 transmission electron microscope with an accelerating voltage of 200 kV. X-ray photoelectron spectroscopy analysis was carried out using a Thermo escalab

250Xi instrument equipped with Al $\text{K}\alpha$ monochromatized X-rays at 1,486.6 eV. Absorption spectra were measured by an ultraviolet–visible spectrophotometer (UV-2450, Shimadzu, Japan). Photoluminescence and radioluminescence spectra were obtained by an Edinburgh FS5 fluorescence spectrophotometer (Edinburgh Instruments Ltd, UK) equipped with a miniature X-ray source (AMPEK, Inc.). Photographs of the X-ray-induced luminescence were acquired with a digital camera (Nikon D7100 with AF Micro-Nikkor 60mm f/2.8D). For the time-resolved photoluminescence measurements, a pulsed excitation source was used. The scintillation decay measurement was carried out at the Institute of High Energy Physics of the Chinese Academy of Sciences with a ^{137}Cs source used for the pulsed excitation. The effective scintillation decay time (τ_{eff}) can be calculated using the following formula:

$$\tau_{\text{eff}} = \frac{1}{I_0} \int_0^{\infty} I(t) dt$$

where $I(t)$ and I_0 denote the radioluminescence (or photoluminescence) intensity as a function of time, t , and the maximum intensity, respectively.

Measurement of photoluminescence quantum yield. The quantum yield was determined with an optical spectrometer equipped with an integrating sphere. Perovskite QDs were dispersed in cyclohexane. The excitation and luminescence emission were detected by a photomultiplier tube (PMT) through total internal reflection in the integration sphere. The photoluminescence quantum yield (PLQY) was calculated according to $\text{PLQY} = P_{\text{sample}} / (S_{\text{ref}} - S_{\text{sample}})$, where S_{ref} and S_{sample} are the excitation light intensities by the solvent and the sample, respectively, and P_{sample} is the integrated emission intensity of the sample (Extended Data Fig. 5e).

Measurement of exciton binding energy in perovskite nanocrystal scintillator. The exciton binding energy (E_a) was estimated by measuring the temperature-dependent radioluminescence intensity. By fitting data derived from the integrated luminescence intensity of the CsPbBr_3 QD scintillator with the Arrhenius formula:

$$I(T) = \frac{I(T_0)}{1 + C T \exp[-E_a / (k_B T)]}$$

where $I(T_0)$ is the radioluminescence intensity at the low-temperature (T_0) limit, k_B is the Boltzmann constant, C is a constant and T is the temperature, we obtain an exciton binding energy of 49 meV.

Fabrication of perovskite nanocrystal scintillator films on PDMS substrates. The PDMS substrates were fabricated by a standard soft lithography microfabrication technique. Briefly, a photomask was first designed using Adobe Illustrator CS6. A 60- μm -thick layer of negative photoresist (SU-8 2015; 2,500 r.p.m., 60 s) was spin-coated onto a silicon wafer (3 inch; 1 inch = 1.54 cm). The wafer was prebaked at 60 °C for 10 min and then at 85 °C for 5 min. The resulting photoresist on the wafer was irradiated by an ultraviolet lamp for 20 s, followed by a post-baking treatment in an oven at 75 °C for 5 min. Next, the desired microstructure on the silicon wafer was produced using a developer solution. The PDMS substrates were fabricated with a premixed PDMS prepolymer and curing agent (10:1 by mass) under vacuum conditions, followed by heat treatment at 80 °C for 2 h. The PDMS replicas were carefully peeled off from the master. Finally, perovskite QDs dispersed in cyclohexane were coated onto the PDMS substrate.

Radioluminescence measurement for perovskite nanocrystal scintillators. The measurement of X-ray-induced luminescence was performed using a solid film comprising perovskite QDs. We note that perovskite QDs dispersed in solution are not suitable for scintillation characterization under X-ray excitation, because a low population of QDs in solution is inefficient for X-ray absorption. Unlike under visible-light excitation, a quartz cuvette is not used for measuring scintillation luminescence under X-ray excitation, because the excitation can be strongly absorbed by the cuvette. The scintillation decay times³⁶ of CsI:Tl, $\text{Bi}_4\text{Ge}_3\text{O}_{12}$, YAlO_3 :Ce and PbWO_4 crystal scintillators are listed in Extended Data Table 1.

X-ray photoconductor devices. To fabricate the X-ray photoconductor device, silica wafers with a 300-nm-thick SiO_2 layer were first cleaned by sonication in acetone, ethanol and deionized water separately. After drying with flowing nitrogen, the substrates were treated with oxygen plasma for 6 min. The solution of CsPbBr_3 QDs was spin-coated onto the Si/SiO_2 substrates at 500 r.p.m. for 30 s and subsequently annealed at 100 °C for 5 min. This procedure was repeated three times to produce a film with a thickness of about 10 μm . After that, 100-nm-thick gold electrodes were deposited onto the CsPbBr_3 QD film by thermal evaporation, using a shadow mask to control the size of the deposition. For the X-ray photon-to-current measurement, we used a commercially available, miniaturized X-ray tube (Amptek). The target in the X-ray tube was made of gold and the maximum output was 4 W. In our measurement, the X-ray tube voltage was kept at 50 kV while the peak X-ray energy was set at 10 keV with an Al/W filter and a 2-mm-diameter brass collimator. The distance between the X-ray source and the X-ray photoconductor device was about 30 cm. The current–voltage measurement of the devices was

performed using a Signotone Micromanipulator S-1160 probe station equipped with a Keithley 4200 Semiconductor Parametric Analyzer. All the experiments were carried out at ambient conditions.

X-ray scintillation detector and imaging. The X-ray scintillation detector was constructed by coating of a PDMS substrate with perovskite QDs (layer thickness of 120 μm), followed by the attachment of a PMT. In a typical procedure, a solution of CsPbBr₃ QDs was spin-coated onto the PDMS substrate. The PDMS substrate was then coupled to the PMT for maximized collection of visible photons. For X-ray detection, a range of X-ray dose rates (0.013–278 $\mu\text{Gy s}^{-1}$) was applied by adjusting the current and voltage of the X-ray source. For X-ray imaging, a plastic disk coated with CsPbBr₃ nanocrystals was used. A green scarab beetle implanted with a metallic needle was employed as a specimen for X-ray imaging.

In vivo multicolour optical bioimaging. All the animal experiments were performed in compliance with institutional guidelines. Silica-coated perovskite QDs (CsPbBr₃, CsPbBr_{1.5}I_{1.5}, CsPbBr_{1.2}I_{1.8}; 100 μg , 50 μl) dispersed in a phosphate-buffered saline buffer solution were subcutaneously injected into the Balb/c nude mice (age, 4–6 weeks; weight, 18 g). An animal imaging system (Advanced Molecular Imager, Cold Spring Biotech Corp., Shanghai) equipped with an X-ray source was used to carry out in vivo radioluminescence imaging of the mice. The exposure time for in vivo imaging was set at 1 s. For in vivo multicolour optical imaging, optical filters (530 nm, 630 nm and 670 nm) were used to selectively record the X-ray-induced luminescence at different emission wavelengths (Extended Data Fig. 11).

Construction of perovskite-based flat-panel X-ray imaging system. The α -Si photodiode assay backplane was customized for commercial α -Si/CsI:Tl detectors supplied by iRAY Technology Shanghai, Inc. The active area of a photodiode array is 43.0 cm \times 43.0 cm, consisting of 3,072 \times 3,072 square pixels with a pixel pitch of 139 μm . CsPbBr₃ nanocrystals were first dispersed in cyclohexane. We coated the photodiode arrays (8.0 cm \times 8.0 cm) with a thin film (thickness, 75 μm) of nanocrystals using a solution-processing method. After evaporation of cyclohexane, an aluminium film (40 μm thick) was added under vacuum, in a packaging process similar to that used in commercial CsI:Tl-based X-ray imaging systems. The aluminium film was used to protect the scintillators from moisture and light soaking. We note that a reflecting layer was coated on the surface of the aluminium film to enhance the light collection into the photodiode elements. The power consumption was 25 W for full-image acquisition and the X-ray source was operated at a voltage of 70 kV. X-ray imaging of electronic circuit boards was acquired with an X-ray exposure of 2.5 mGy s^{-1} for 6 ms, resulting in a dose of 15 μGy . The spatial resolution was determined by measurement of the modulation transfer function.

Radioluminescence analysis using synchrotron radiation. The characterization of the yield of X-ray-induced luminescence near electronic-shell edges was conducted using the synchrotron beamline in the Shanghai Synchrotron Radiation Facility. A thin film of CsPbBr₃ nanocrystals was cast onto a PDMS substrate. The X-ray excitation energies were 10–38 keV, and a portable spectrophotometer (Ocean Optics) was used to measure the radioluminescence.

Density functional theory calculation. For the calculation of the projected partial density of states (PDOS), density functional theory (DFT) calculations were carried out. We used the Cambridge Serial Total Energy Package (CASTEP) source code to perform the calculations with the rotation-invariant DFT+U method. In a typical procedure, a simple cubic phase with $Pm\bar{3}m$ symmetrical lattice arrangement was modelled for bulk-phase CsPbBr₃. Norm-conserving pseudopotentials of the Cs, Pb and Br atoms were generated by the OPIUM code in the Kleinman–Bylander projector form. A nonlinear partial core correction and a scalar relativistic averaging scheme were used to treat the spin–orbit coupling effect. In particular, we treated the 4s, 4p and 4d states of the Br atoms as valence states, the 5s, 5p and 5d states for Cs atoms, and the 5d, 6s and 6p states for Pb atoms. The Rappe–Rabe–Kaxiras–Joannopoulos method was chosen to optimize the pseudopotentials during electronic minimization, particularly using a blocked-Davidson-scheme matrix diagonalization.

For the calculations of the electronic states in the CsPbBr₃ material, we used self-consistent determination for on-site U correction on the localized *p* orbitals of Br sites to correct the on-site Coulomb energy of the electron spurious self-energy. The on-site electronic self-energy and related wavefunction relaxation in the semicore *p*, *d* or *f* orbitals in mixed-valence elements were used to obtain accurate orbital eigenvalues for the electronic structures and transition levels. An ab initio two-way crossover searching calculation was performed by two functionally compiled CASTEP-17 source codes. Using the self-consistent determination, on-site Hubbard U parameters for different orbitals of Br and Pb sites were obtained. Further, a time-dependent DFT calculation was performed with a two-electron-based Tamm–Dancoff approximation imported from the self-consistently corrected ground-state wavefunctions.

Luminescence mechanisms in perovskite nanocrystal scintillator. Two energy-transfer mechanisms for recombination luminescence exist in the perovskite nanocrystal scintillator. One is anisotropic electron and hole transport within the

reciprocal Brillouin zone, which leads to a difference between the electron effective mass along different paths and the excitonic binding energy. This difference illustrates the probability that electronic transport within reciprocal band structures is directionally selected for luminescence. Another plausible route is the annihilation of shallow acceptor levels (Pb vacancies), which induces an absence of recombination centres. Such intrinsic lattice defects usually produce low-excitation energy levels compared with the ideal lattice and consequently hinder energy transfer during the light-absorption process.

Anisotropic transport-induced luminescence contrast. Using DFT calculations, the bandgap of a bulk CsPbBr₃ crystal was calculated to be about 2.02 eV, whereas in the CsPbBr₃ QDs the bandgap increases slightly to 2.22 eV (Fig. 2d). This is because the large surface-to-volume ratio in the CsPbBr₃ nanocrystal induces an evident quantum confinement, thus leading to an enlarged vacuum Coulomb barrier for electronic transitions.

We chose reciprocal, highly symmetrical points and lined up two different paths ($X \rightarrow R \rightarrow M \rightarrow \Gamma \rightarrow R$ and $\Gamma \rightarrow R \rightarrow M$) within the Brillouin zone. As shown in the electronic band structure plot in Fig. 2d, the valence band edge and the conduction band edge are located at the same point $R(1/2, 1/2, 1/2)$. Using effective mass theory, the effective mass for electrons and holes was found to be anisotropic along these two directions. In the directions $X \rightarrow R \rightarrow M \rightarrow \Gamma \rightarrow R$ and $\Gamma \rightarrow R \rightarrow M$, the effective masses for electrons were calculated to be 0.03 m_0 and 0.11 m_0 and the effective masses for holes were calculated to be 0.12 m_0 and 0.24 m_0 , respectively, where m_0 is the rest mass of the electron. Thus, the Wannier–Mott exciton binding energy and radius are different in these two directions.

By converting the reciprocal Brillouin zone area into a real-space diagram, we found that the Cs site at $\Gamma(0, 0, 0)$ in the body-centred area is different in these two paths. Point $R(1/2, 1/2, 1/2)$ denotes the position of the Pb site, whereas $M(1/2, 1/2, 0)$ represents the location of the Br site. Owing to the different effective electron masses of the two paths, the path $\Gamma \rightarrow R \rightarrow M$ is energetically favourable to the transport of electrons and holes. By contrast, the $X \rightarrow R \rightarrow M$ direction is ruled out because the binding energies are too large to release electrons and holes for recombination. This implies a charge transfer process from the Cs site to the Pb site at the cubic apex point, finally reaching the Br site at the middle point of the cubic edge, namely, through the path $\Gamma \rightarrow R \rightarrow M$ (Extended Data Fig. 7a).

Furthermore, we used an orbital calculation to retrieve the electronic and hole orbitals from the electronic band structure. Our results show that bound electrons stay at the Br sites at a non-bonding state in the *p*– π orbital level (Extended Data Fig. 7b). Meanwhile, bound holes were found to stay at the Pb site with an *s*-orbital spherical distribution (Extended Data Fig. 7c). The orbital contour plots reveal the localization of electrons and holes at perfect lattices. The stabilized charge state of the body-centred Cs site is Cs^+ because electrons are transferred from the Pb site to the Br site through the ionization of one *s*-state electron.

Intrinsic lattice defects in perovskite nanocrystal scintillators. Intrinsic lattice defects in perovskite nanocrystal scintillators are responsible for both luminescence and the quenching effect. Here we consider the low-energy native defects of a Br vacancy (V_{Br}) and a Pb vacancy (V_{Pb}). For V_{Br} , the absence of one Br atom leaves one electron occupying the empty *p* orbitals of the nearest neighbouring Pb site. Accordingly, localized electronic orbitals were modelled for V_{Br} in the neutral (V_{Br}^0) and singly positive (V_{Br}^+) states (Extended Data Fig. 7d, e). Because the charge bound at the nearby Pb site is positively ionized, the *p* electronic orbitals of the V_{Br}^+ site show a transition from the correlated state to a repulsive behaviour between the two neighbouring Pb sites. The PDOS analysis also shows that the electronic level of V_{Br} , which is localized at the bottom of the conduction band edge, serves as a shallow donor. The V_{Pb} lattice defects produce an acceptor trap centre and a spin-polarized state (Extended Data Fig. 7f, g). The singly negative state of a Pb site (V_{Pb}^-) with one electron already captured could partially passivate the acceptor trap site with weakened charge localization. The process of local geometrical relaxation on different charge states of V_{Pb} indicates that the Cs^+ sites centrosymmetrically move towards the V_{Pb} centre (Extended Data Fig. 7h). Upon the occurrence of a strong clustering effect to form V_{Pb}^{2-} near the V_{Pb} site, the electronically active acceptor trap centre can be completely terminated. In this case, formation of local Cs–Br motifs is possible. We also considered V_{Cs} and V_{Cs}^- sites in the lattice and found no effects on the electronic properties of the host lattice. Accordingly, V_{Br} and V_{Pb} produce the electronic and hole levels for luminescence recombination in the form of photon emission (Extended Data Fig. 7i).

Further, we calculated the excited energy and thermodynamic transition levels in the CsPbBr₃ QDs. From the internal bulk lattice to the surface region, the dimensions of the material decrease but its surface-to-volume ratio is increased. The electronic donor trap levels experience a transition from a localized state below the conduction band edge to a delocalized state in the conduction band (Extended Data Fig. 7j). During the process of radiation ionization and release, the number of bound electrons is increased accordingly. By contrast, with a decreased dimension of the host lattice, the trapping ability of the acceptor is decreased where the hole level shifts from a delocalized state in the valence band to a localized state above

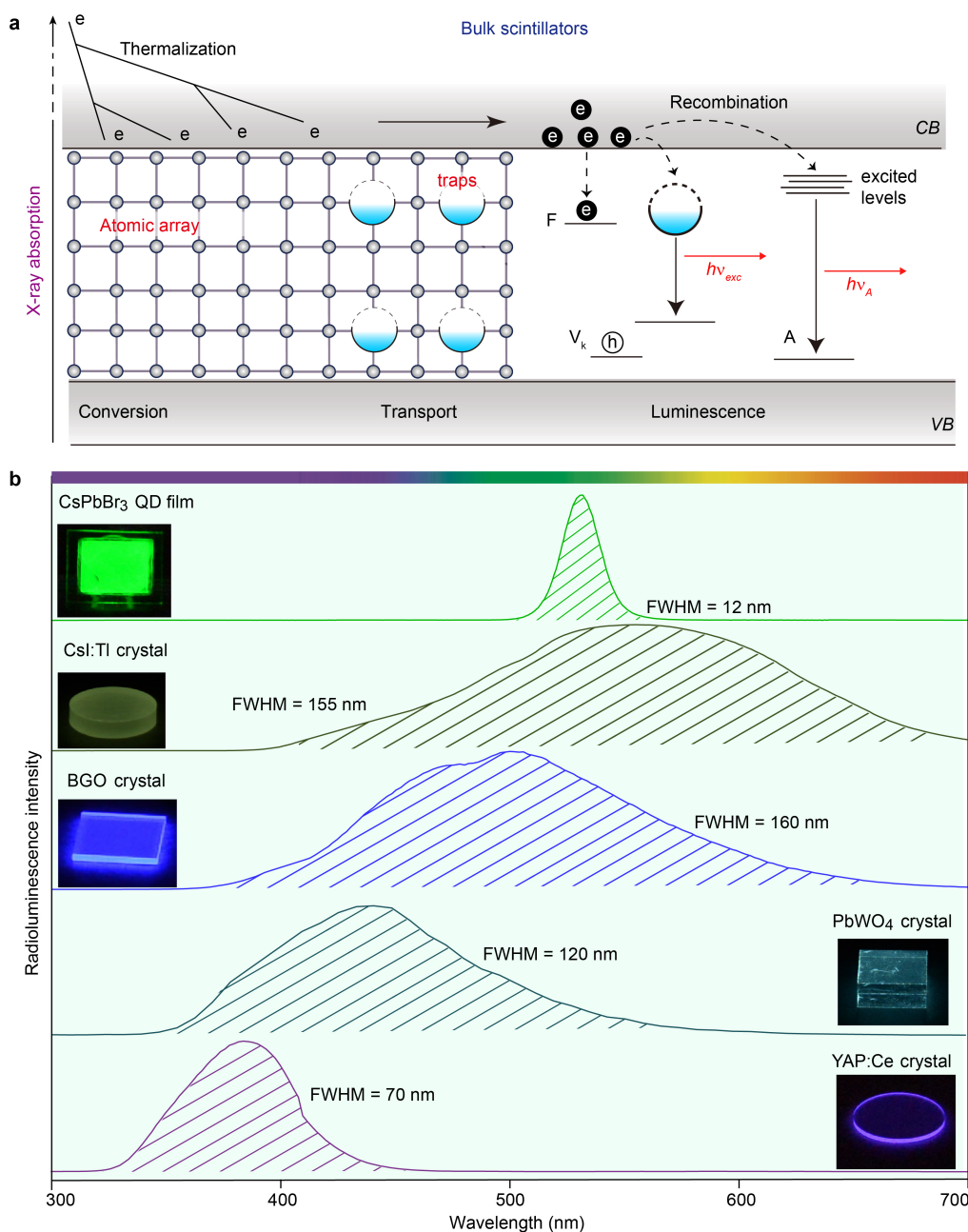
the valence band. Therefore, the quenching effect in the bulk CsPbBr₃ materials for luminescence recombination is caused by annihilation of a hole level that is deeply buried in the valence band. The structural transition from the QD to the bulk form occurs from the surface to the bulk, thus the hole level is annihilated.

Intrinsic quantum confinement in CsPbBr₃ nanocrystals. The intrinsic effect of quantum confinement in CsPbBr₃ nanocrystals was examined by additional theoretical study of their surface electronic properties. In a typical procedure, we first built a simplified model of the CsPbBr₃ structure composed of 293 atoms with a particle size of 12.06 Å, namely, a lattice group (6 × 6 × 6) truncated from bulk CsPbBr₃ crystal, using the radial coordinated structural formation program (RCSFP) (Extended Data Fig. 8a). DFT calculations yield that the orbital contour plots of the CsPbBr₃ QD show the highest occupied molecular orbital (HOMO), the lowest unoccupied molecular orbital (LUMO) and surface-vacancy-induced Coulomb trapping (SVIC) states (Extended Data Fig. 8b). The electronic structures show that the SVIC state is formed owing to unsaturated *p* orbitals of surface Br sites and is electronically localized at the apex corner regions of the QD. Additionally, the PDOS of the CsPbBr₃ QD indicates that such SVIC sites are mainly distributed near the Fermi level, beyond the valence band maximum, thus exhibiting a hole-like feature and being strongly confined by the LUMO orbitals (Extended Data Fig. 8c). This leads to the suppression of the long-distance transport of electron–hole pairs across the particle surface or between particles. Furthermore, a model was built to perform a simulation of the energetic evolution

on the surface of the QDs as a function of particle distance (Extended Data Fig. 8d). To investigate surface confinement, we further calculated the relative energy level of the SVIC state as a function of particle distance (Extended Data Fig. 8d). It is obvious that at a distance of 12.06 Å from the particle surface, the SVIC energy implies a strong hole-like confinement, merely 0.056 eV above the valence band maximum. Our results suggest that the mean confinement path of electronic transport within the lattice is approximately 10.32 Å (Fig. 2f). Indeed, the intrinsic energetics on the surface of the QDs is reasonable for energy confinement of the thermalized low-energy excitons inside the nanocrystal, resulting in a high yield of X-ray scintillation light.

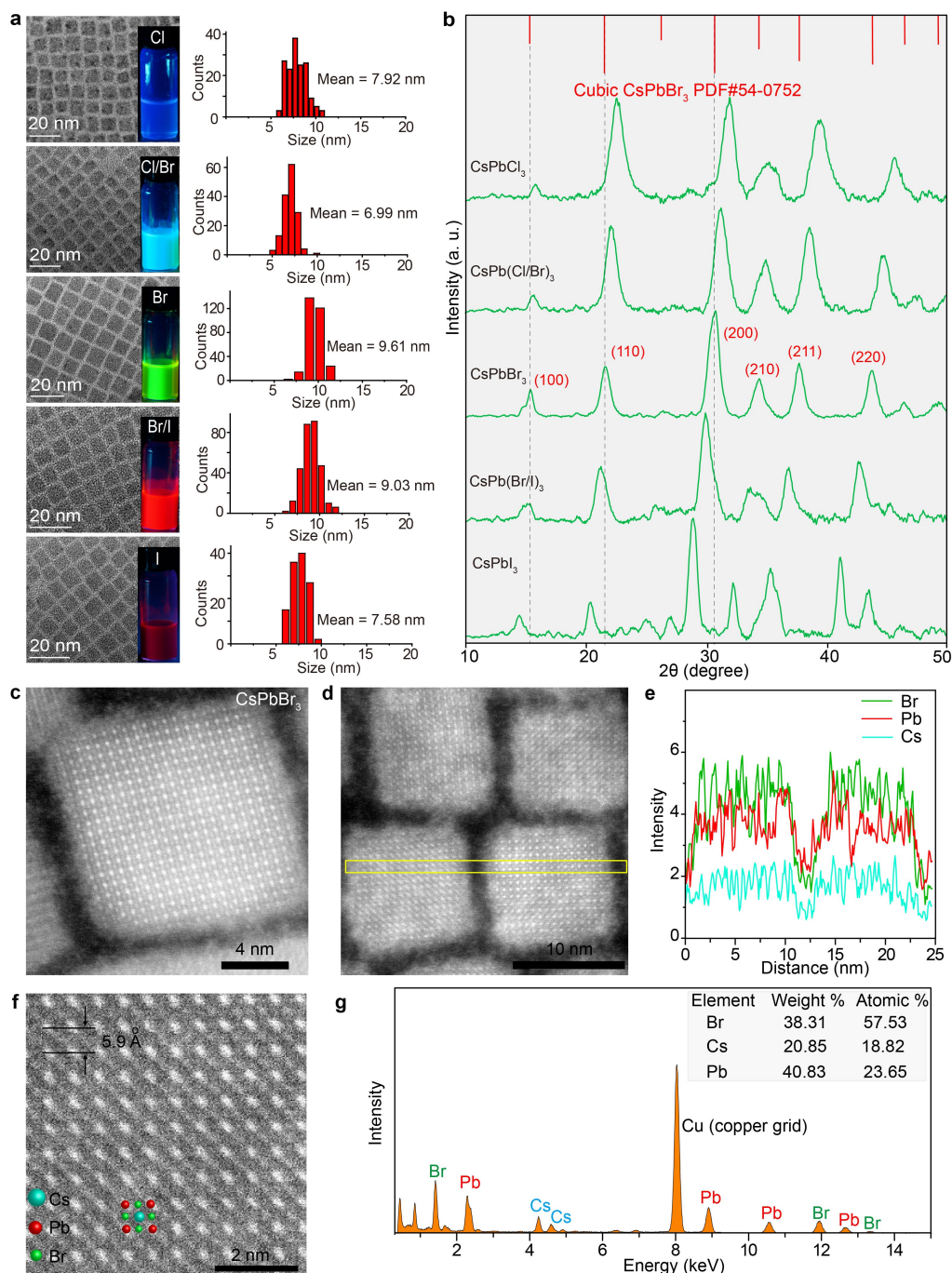
Data availability. The data that support the findings of this study are available from the corresponding authors upon reasonable request.

34. Saidaminov, M. I. et al. Inorganic lead halide perovskite single crystals: phase-selective low-temperature growth, carrier transport properties, and self-powered photodetection. *Adv. Opt. Mater.* **5**, 1600704 (2017).
35. Huang, S. et al. Enhancing the stability of CH₃NH₃PbBr₃ quantum dots by embedding in silica spheres derived from tetramethyl orthosilicate in “waterless” toluene. *J. Am. Chem. Soc.* **138**, 5749–5752 (2016).
36. Nikl, M. Scintillation detectors for X-rays. *Meas. Sci. Technol.* **17**, 37–54 (2006).
37. Miyata, A. et al. Direct measurement of the exciton binding energy and effective masses for charge carriers in organic–inorganic tri-halide perovskites. *Nat. Photon.* **11**, 582–587 (2015).



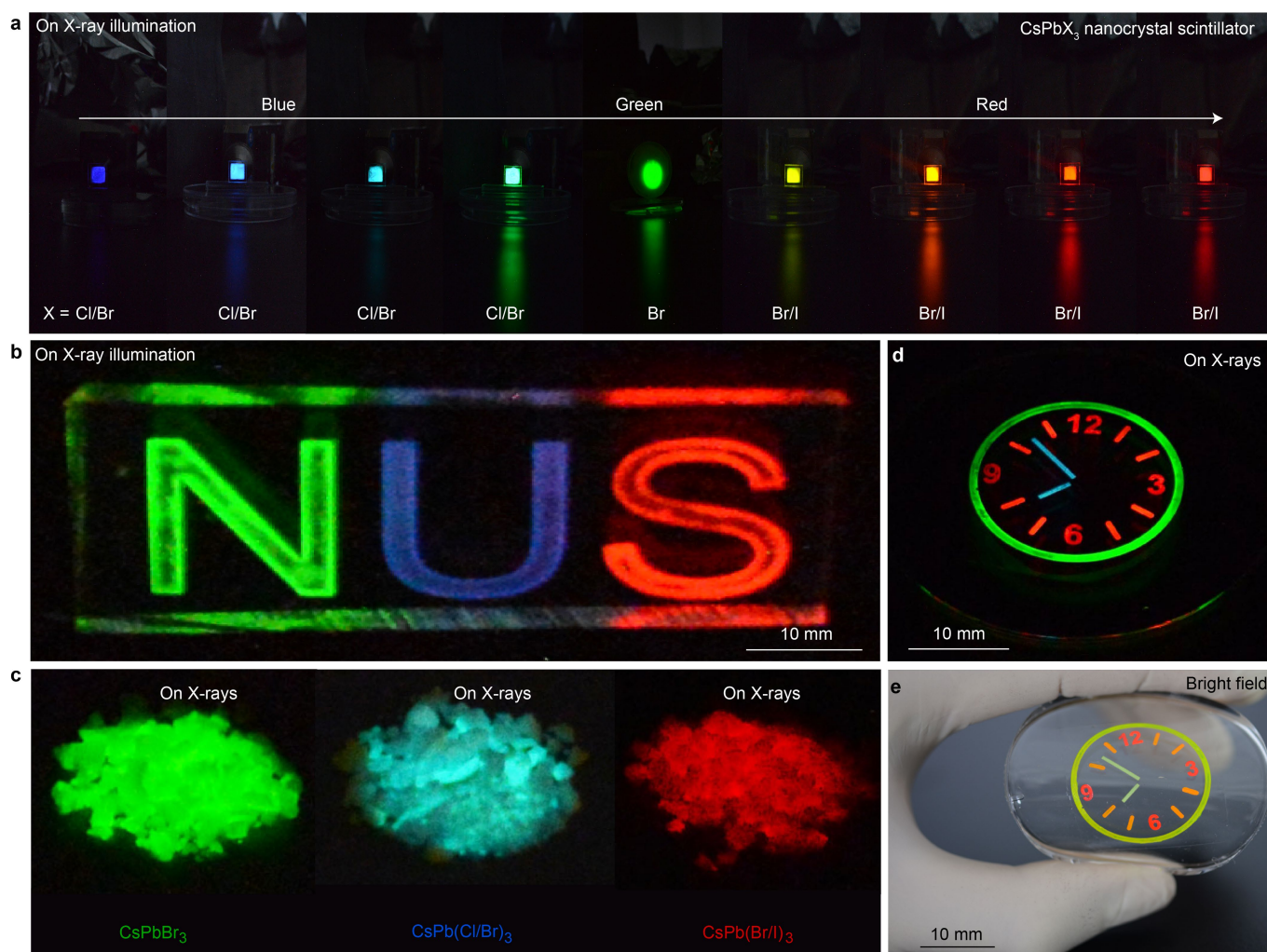
Extended Data Fig. 1 | Schematic representation of scintillation mechanism and X-ray-induced luminescence in bulk inorganic scintillators. a, In bulk inorganic materials, X-ray photons absorbed by the lattice atoms can generate hot charge carriers, followed by exciton thermalization and subsequent transport to defect sites or activator centres ('traps'), where radiative emission occurs. VB, valence band; CB, conduction band; V_k , self-trapped hole; F, Farbe centre; ν_{exc} , photon

frequency during excitonic luminescence; ν_A , photon frequency during activator (A) luminescence. **b**, Scintillation properties of CsPbBr₃ QDs and commercial bulk inorganic materials under X-ray excitation. The full-width at half-maximum (FWHM) represents the spectral width of the scintillation spectra of the crystal. The insets show photographs of the corresponding samples acquired under X-ray excitation. BGO, Bi₄Ge₃O₁₂.



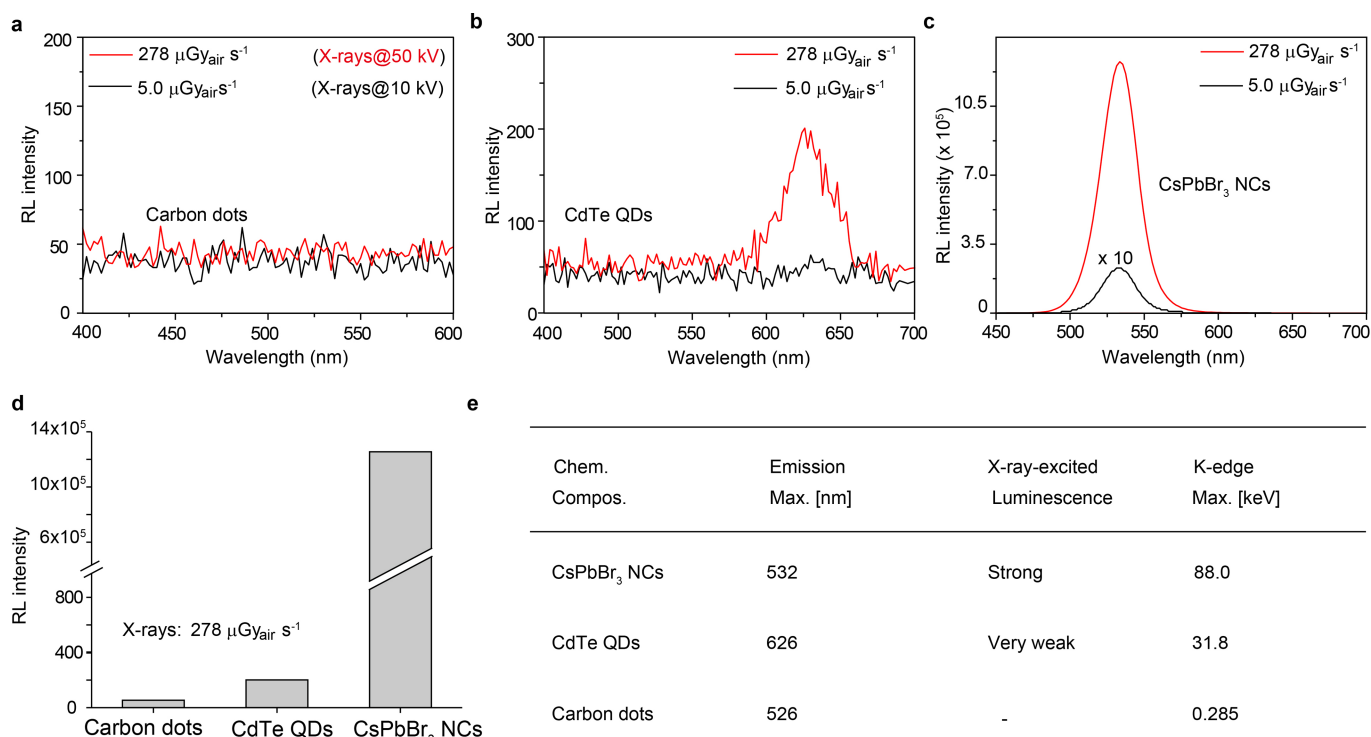
Extended Data Fig. 2 | Physical characterization of as-synthesized perovskite QDs. **a**, TEM images of the as-prepared cubic-phased nanocrystals (left) and the corresponding size distribution of the nanocrystals (right). The samples are CsPbCl₃, CsPb(Cl/Br)₃, CsPbBr₃, CsPb(Br/I)₃ and CsPbI₃ nanocrystals (from top to bottom). Insets are images of perovskite nanocrystals dispersed in cyclohexane, recorded under 365-nm ultraviolet light excitation. **b**, Powder X-ray diffraction patterns for typical ternary and mixed-halide CsPbX₃ (X = Cl, Br or I) nanocrystals. All peaks are indexed in accordance with the cubic-phased CsPbBr₃ structure (Joint Committee on Powder Diffraction Standards file

(PDF) number 54-0752). **c**, **d**, Dark-field scanning transmission electron micrographs (STEM; JEM-F200HR) of CsPbBr₃ nanocrystals. **e**, Elemental mapping of Br, Pb and Cs for the nanocrystals, obtained from the area marked by the rectangular box in **d** using energy-dispersive X-ray spectroscopy. **f**, Atomically resolved dark-field STEM image of a single CsPbBr₃ nanocrystal, showing Cs and Pb lattice atoms. **g**, Energy-dispersive X-ray spectrum of the as-prepared CsPbBr₃ perovskite nanocrystals, confirming the stoichiometric composition of the CsPbBr₃ nanocrystals. We note that strong Cu signals come from the TEM copper grid.



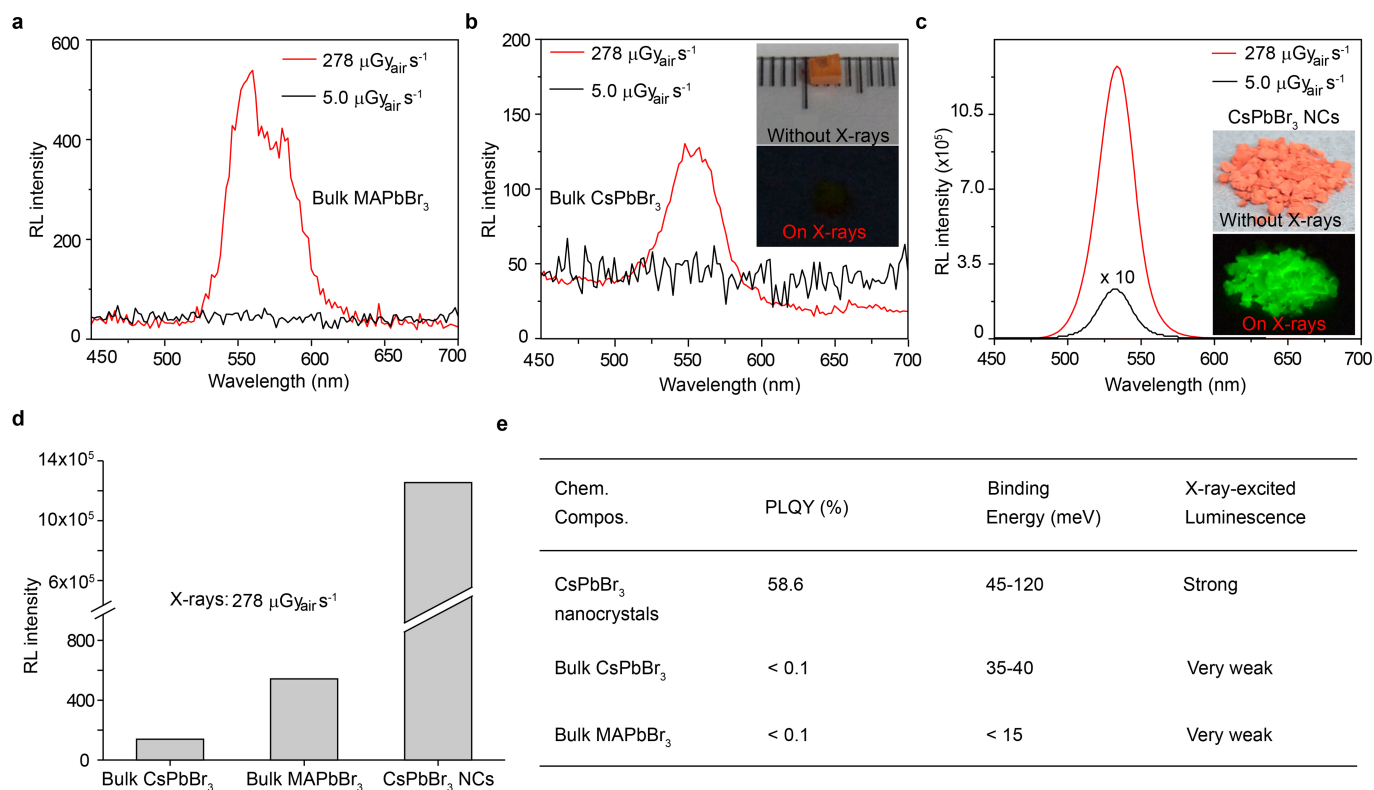
Extended Data Fig. 3 | Multicolour-emitting perovskite QD scintillators upon X-ray irradiation. **a**, Demonstration of X-ray-induced luminescence modulation using CsPbX_3 QDs of different compositions ($X = \text{Cl}, \text{Br}$ or I). **b**, Multicolour X-ray scintillation from $\text{CsPb}(\text{Cl}/\text{Br})_3$, CsPbBr_3 and $\text{CsPb}(\text{Br}/\text{I})_3$ nanocrystals cast on a PDMS substrate. The X-ray dose rate is

$278 \mu\text{Gy s}^{-1}$. **c**, Typical photographs of radioluminescence from $\text{CsPb}(\text{Cl}/\text{Br})_3$, CsPbBr_3 and $\text{CsPb}(\text{Br}/\text{I})_3$ QDs under X-ray excitation. **d, e**, Multicolour visualization of as-developed perovskite QD scintillators using X-rays (**d**) and the corresponding bright-field image (**e**).



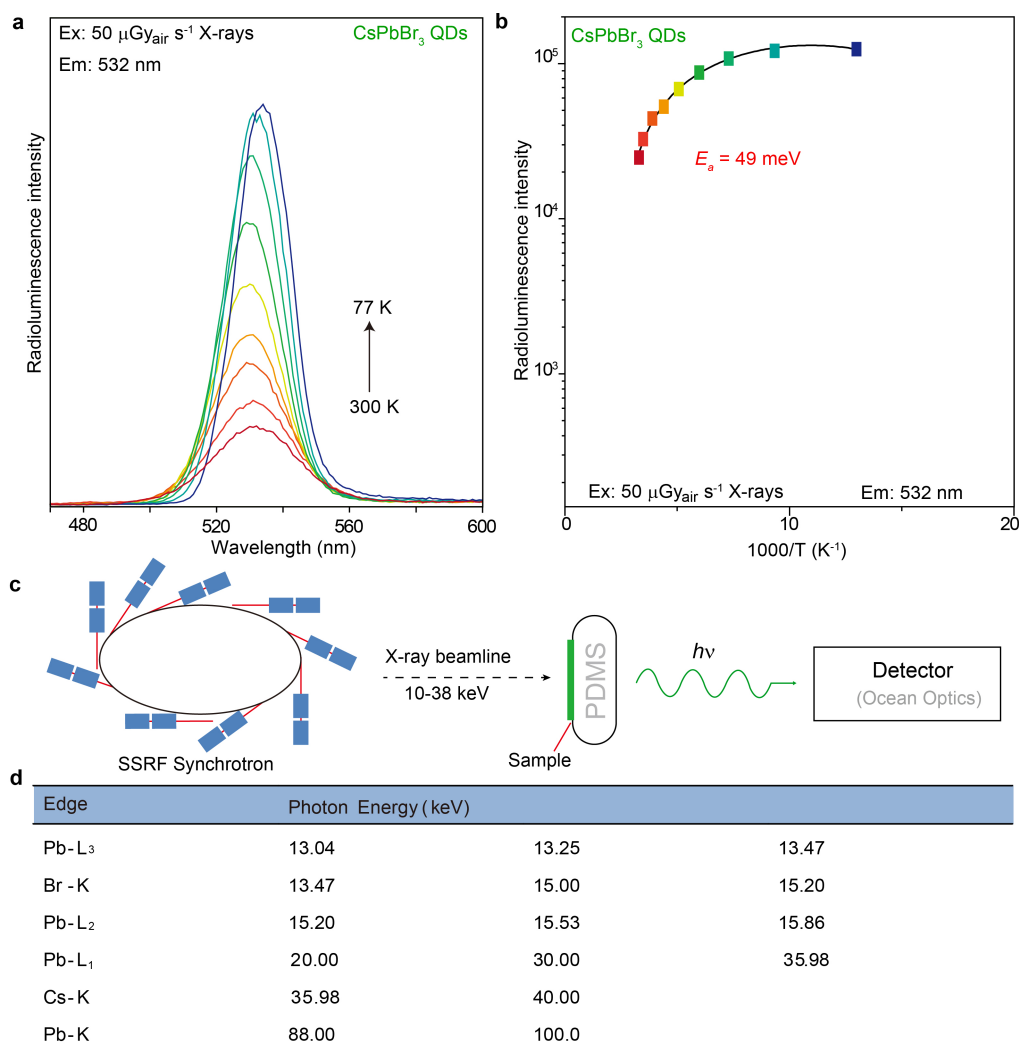
Extended Data Fig. 4 | Comparison of X-ray-induced luminescence intensity for QDs. **a–c**, Radioluminescence spectra of carbon dots (**a**), CdTe QDs (**b**) and CsPbBr₃ nanocrystals (NCs; **c**) under X-ray excitation at 5.0 $\mu\text{Gy} \text{s}^{-1}$ and 278 $\mu\text{Gy} \text{s}^{-1}$. **d**, Comparison of radioluminescence

intensity for the as-prepared carbon dots, CdTe QDs and CsPbBr₃ nanocrystals under 278 $\mu\text{Gy} \text{s}^{-1}$ X-ray excitation. **e**, Scintillation performance and maximal K-edge energy of lead halide perovskite nanocrystals, carbon dots and CdTe QDs.



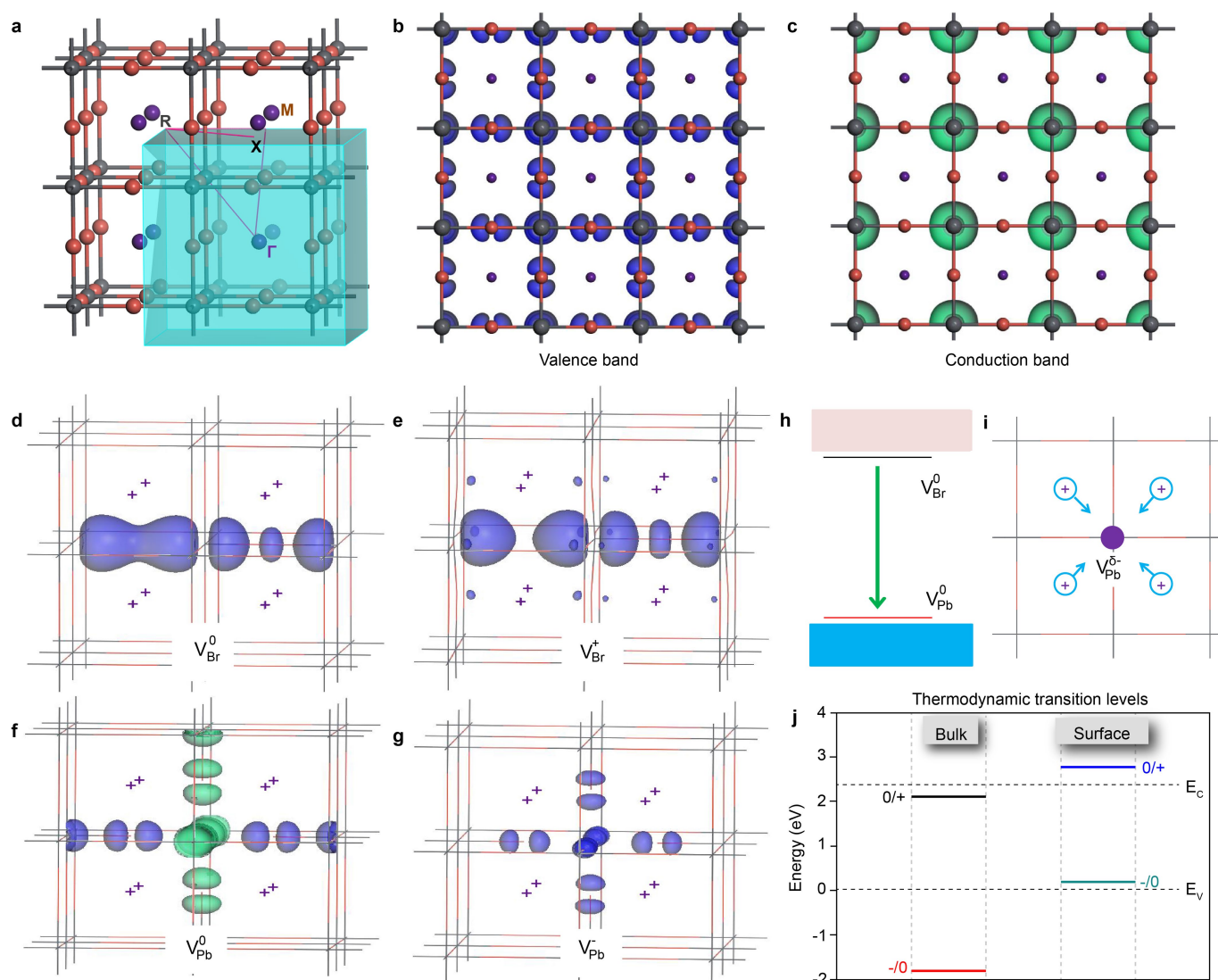
Extended Data Fig. 5 | Comparison of X-ray-induced luminescence for lead halide perovskite materials. **a–c**, Radioluminescence spectra of bulk single-crystal $\text{CH}_3\text{NH}_3\text{PbBr}_3$ (**a**) and CsPbBr_3 (**b**) and of CsPbBr_3 nanocrystals (**c**) under X-ray excitation at $5.0 \mu\text{Gy s}^{-1}$ and $278 \mu\text{Gy s}^{-1}$. The insets are photographs of CsPbBr_3 bulk single crystal (**b**) and nanocrystal powders (**c**) taken under ambient light (top) and X-ray illumination (bottom). The X-ray dose used for the experiments was

$278 \mu\text{Gy s}^{-1}$. **d**, Comparison of radioluminescence intensity for three types of perovskite material under $278 \mu\text{Gy s}^{-1}$ X-ray excitation. **e**, PLQY and exciton binding energy of perovskite materials at 300 K^{31,37}. We note that the thermal energy at 300 K is $k_B T \approx 25$ meV. Nanocrystalline perovskites are highly luminescent materials, whereas bulk perovskite crystals are most suitable for the generation of free charge carriers owing to their low exciton binding energy.



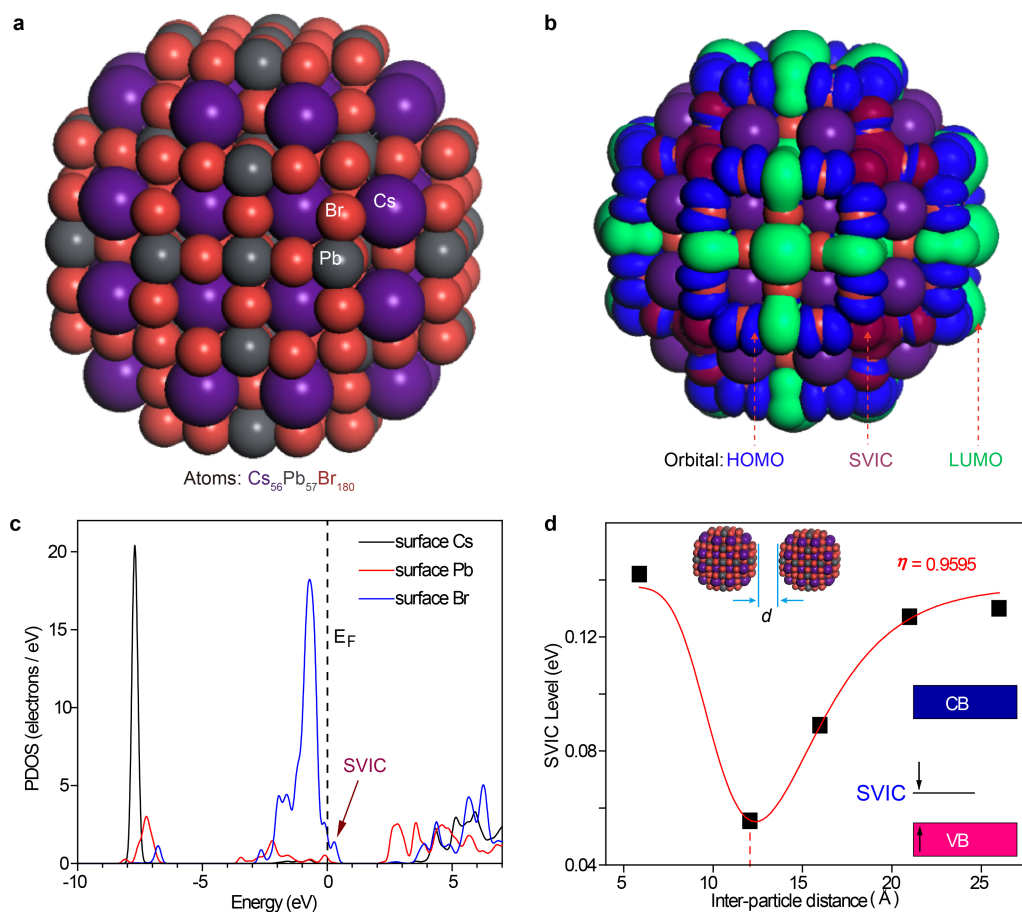
Extended Data Fig. 6 | Measurement of exciton binding energy and synchrotron-radiation-induced radioluminescence of CsPbBr₃ nanocrystals. **a**, Temperature-dependent scintillation spectra of the CsPbBr₃ nanocrystals at 77–300 K under X-ray illumination at $50 \mu\text{Gy} \text{s}^{-1}$. **b**, Arrhenius plot of the X-ray-induced luminescence intensities of

the CsPbBr₃ nanocrystals at 532 nm. **c**, Experimental setup for the synchrotron-radiation-induced radioluminescence measurements at the X-ray beamline of the Shanghai Synchrotron Radiation Facility (SSRF). The X-ray energy is 10–38 keV. **d**, The electronic edge energies for Pb L, Cs K and Br K.



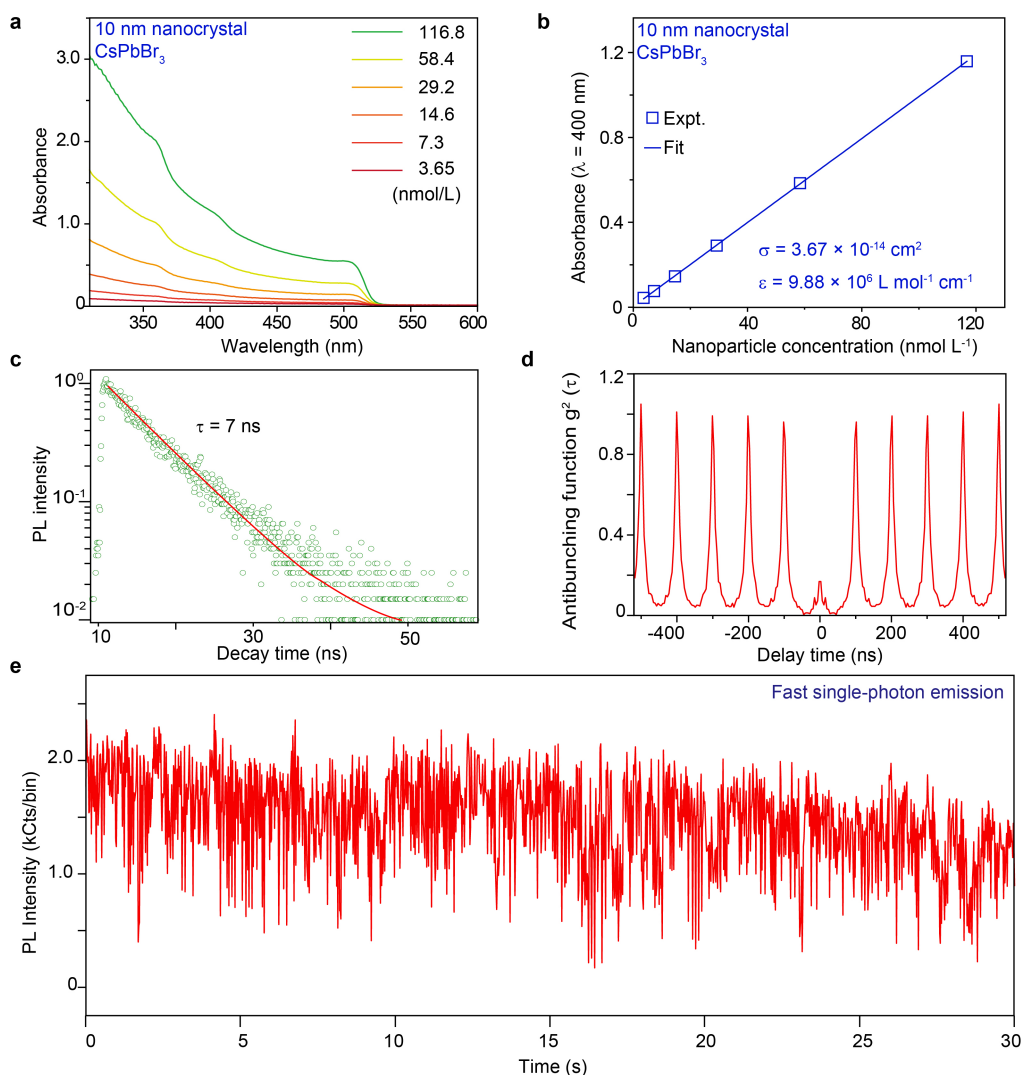
Extended Data Fig. 7 | Electronic structure and scintillation mechanism of the CsPbBr₃ nanocrystal along selected reciprocal high-symmetry points within the Brillouin zone. **a**, The Brillouin zone of the cubic-phased crystal lattice in CsPbBr₃, calculated using relativistic corrections. Γ , M, R and X denote high-symmetry points within the reciprocal space (blue). **b**, **c**, Calculated electron density associated with the valence band (**b**) and the conduction band (**c**) of the cubic CsPbBr₃. We note that the halide ions contribute to the changes of the bandgap in the perovskite

nanocrystal through the influence of the valence orbitals. Cs, purple; Pb, grey; Br, orange; electron orbital, blue; hole orbital, green. **d-g**, Localized electronic and hole levels for V_{Br} and V_{Pb} at different charge states. **h**, **i**, Schematic diagram of energy transfer for radioluminescence induced by intrinsic lattice defects and the quenching effect caused by evident ion movement (Cs^+). $V_{Pb}^{\delta-}$ denotes a Pb vacancy with small ($|\delta| < 1$) charge transfer. **j**, Thermodynamic transition levels of the perovskite nanocrystal. E_c , maximum valence band energy; E_v , minimum conduction band energy.



Extended Data Fig. 8 | Theoretical studies of the surface electronic properties of CsPbBr₃ nanocrystals. **a**, Simplified model of CsPbBr₃ structure composed of 293 atoms with a particle size of 12.06 Å. **b**, Calculated orbital contour plots of a CsPbBr₃ nanocrystal, showing the HOMO (blue), LUMO (green) and SVIC trapping (red) states. The SVIC states are formed owing to unsaturated *p* orbitals of surface Br sites. **c**, PDOS of the CsPbBr₃ QD. The SVIC state is located near the Fermi

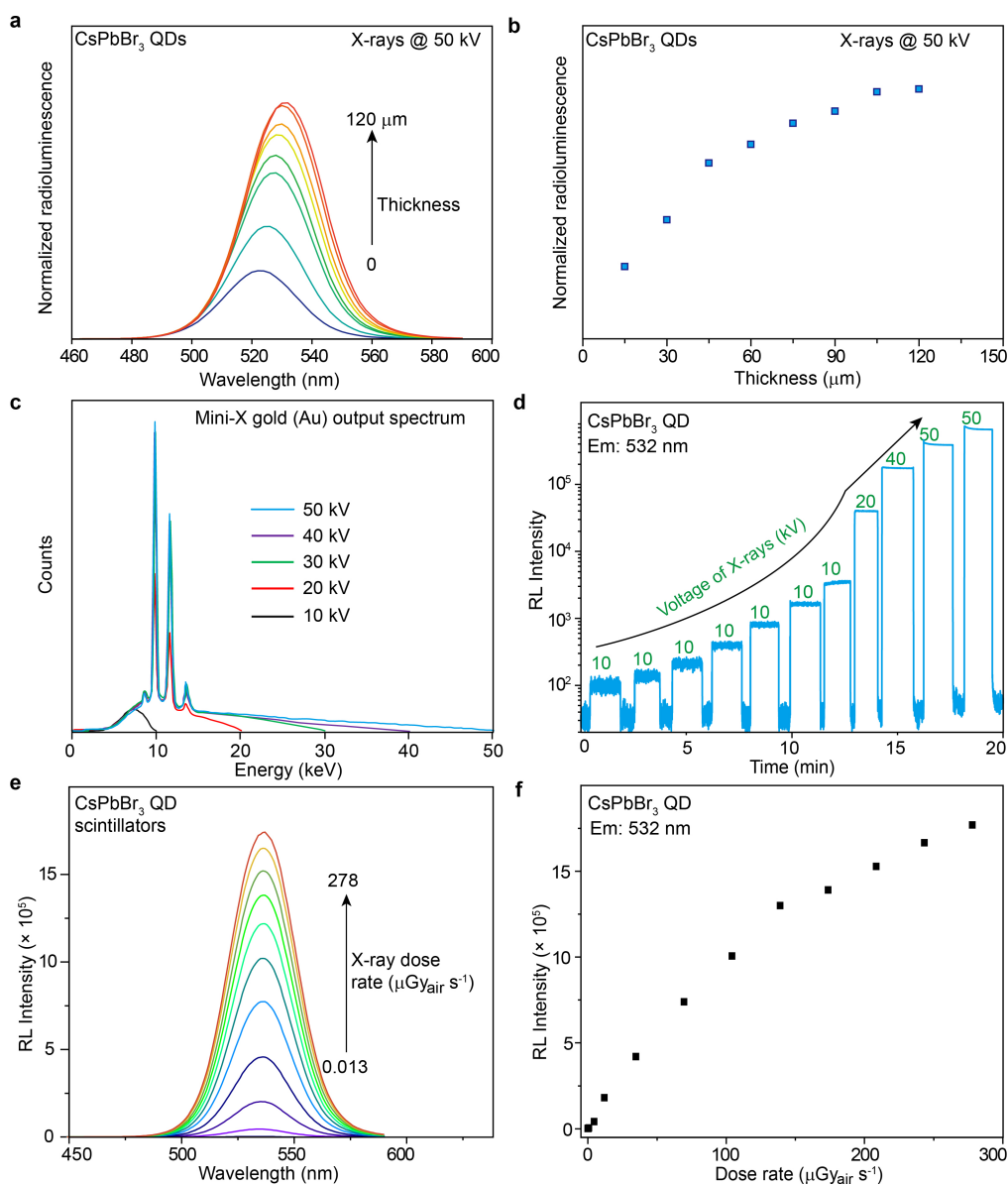
level (E_F). **d**, The relative energy of the SVIC state to the valence band (VB) maximum as a function of inter-particle distance, d . The red line is calculated by fitting with the Gaussian distribution function. The top inset shows the simulation model used to calculate the energy evolution of the CsPbBr₃ nanocrystal as a function of particle distance. CB, conduction band.



Extended Data Fig. 9 | Characterization of absorption cross-section and transient luminescence spectra of the CsPbBr₃ nanocrystals.

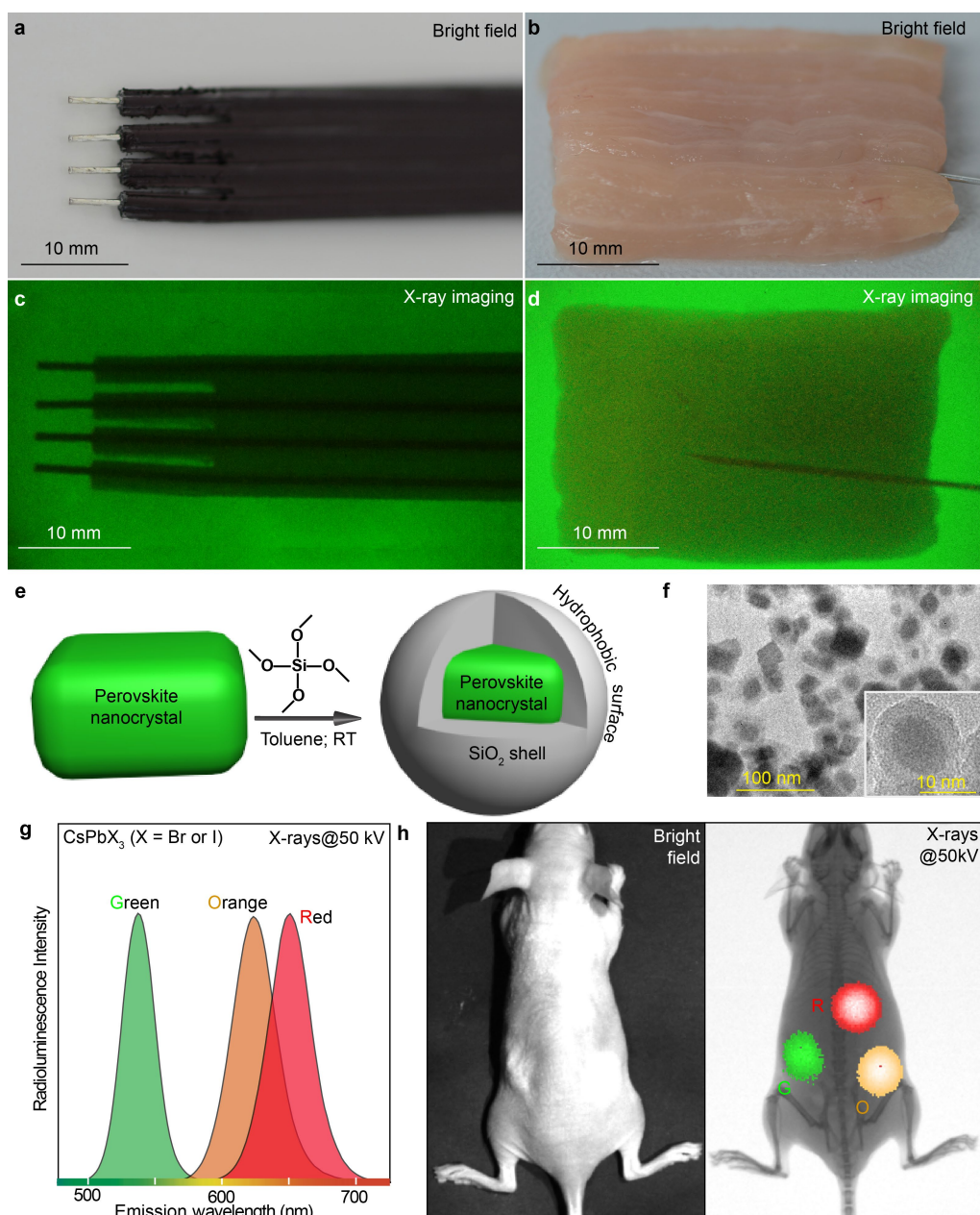
a, Absorption spectra of CsPbBr₃ nanocrystals dispersed in cyclohexane at different concentrations. **b**, Absorption as a function of concentration for CsPbBr₃ nanocrystals. The molar extinction coefficient, ε , was determined by applying the Beer–Lambert law $A = \varepsilon cL$, where A is the absorbance, c is the molar concentration (mol l⁻¹) and L is the optical path length (1 cm) through the sample. The absorption cross-section,

σ , was determined by $\varepsilon = N_A \sigma / (1,000 \times \ln 10)$, where N_A is Avogadro's number. **c**, Photoluminescence (PL) lifetime of a single CsPbBr₃ perovskite nanocrystal. **d**, Second-order correlation function, $g^2(\tau)$, of the nanocrystal. The value $g^2(0) = 0.16$ confirms the single-quantum-emitter nature of the photon emission. **e**, Fluorescence intermittency trace recorded for a single CsPbBr₃ perovskite nanocrystal. The recorded photoluminescence intensity reaches more than 2,000 counts per 20-ms bin.



Extended Data Fig. 10 | Performance of X-ray detection system using CsPbBr₃ nanocrystal scintillators. **a**, Normalized radioluminescence intensity of CsPbBr₃ nanocrystals of different thickness under X-ray excitation at a voltage of 50 kV. **b**, Normalized radioluminescence intensity as a function of perovskite nanocrystal film thickness. **c**, X-ray output spectra recorded at 10, 20, 30, 40 and 50 kV. **d**, Kinetic measurement of

radioluminescence intensity at 532 nm in response to an X-ray dose rate of 0.013–278 $\mu\text{Gy s}^{-1}$. **e**, Emission spectra of CsPbBr₃ nanocrystal scintillator in response to an X-ray dose rate of 0.013–278 $\mu\text{Gy s}^{-1}$. **f**, Radioluminescence (RL) intensity as a function of the X-ray dose rate shown in **e**.



Extended Data Fig. 11 | Direct X-ray imaging and multiplexed labelling for in vivo optical imaging using perovkite nanocrystal scintillators. **a–d**, A flexible flat cable (**a**) and needle-implanted pork tissue (**b**) were imaged with bright-field and X-ray imaging (**c, d**). We note that the CsPbBr₃ nanocrystal scintillator platform shown in Fig. 3d was used for the X-ray phase contrast imaging. In both cases, the X-ray images clearly reveal the presence of metallic wires embedded in the cable and pork tissue. **e**, Synthesis of CsPbBr₃/SiO₂ core-shell nanoparticles with a hydrophobic surface for protection against moisture. RT, room temperature. **f**, TEM image of the as-prepared CsPbBr₃/SiO₂

nanoparticles. **g**, Multicolour luminescence spectra of the perovkite nanocrystals under X-ray irradiation at a voltage of 50 kV. The materials' compositions are CsPbBr₃, CsPbBr_{1.5}I_{1.5} and CsPbBr_{1.2}I_{1.8} for green (G), orange (O) and red (R) emissions, respectively. We note that the risk of lead toxicity must be considered during experimentation. **h**, Bright-field and multicolour luminescent in vivo imaging in mice under X-ray excitation at a voltage of 50 kV. The X-ray-induced luminescence was recorded by a charge-coupled-device camera equipped with three optical filters at 530 nm, 630 nm and 670 nm.

Extended Data Table 1 | Scintillation characteristics for different materials

Chemical Comp.	Emission Max. (nm)	FWHM (nm)	Thickness (mm)	Decay Time (ns)	Synthetic Temp. (°C)
CsPbX ₃ QDs	410-700	12-40	0.1	44.6	~160
CsI:Tl	565	155	5.0	1000	~1700
Bi ₄ Ge ₃ O ₁₂	490	160	3.0	300	~1700
YAlO ₃ :Ce	380	55	0.6	10 ² -10 ⁴	~1700
PbWO ₄	440	120	5.0	10 ² -10 ⁴	~1700

Extended Data Table 2 | Properties of perovskite nanocrystals and bulk crystals used for X-ray detection

Chemical component	Material type	Electric response	Lumines. response	Multicolor scintillation	Detection limit ($\mu\text{Gy}_{\text{air}} \text{s}^{-1}$)	Imaging method	Remarks
CsPbX ₃ nanocrystals (X=Cl, Br, I)	Scintillator	Low	Highly sensitive	Yes	0.013	Photon-to-photon conversion	<i>This work</i> ^a
MAPbI ₃ thin film	Semiconductor	Good	Not reported	No	~1000	Photon-to-current conversion	<i>Nature Photon.</i> 2015 , 9, 444.
MAPbBr ₃ single crystal	Semiconductor	Excellent	Not reported	No	0.5	-	<i>Nat. Photon.</i> 2016 , 10, 333.
MAPbBr ₃ single crystal/Si substrate	Semiconductor	Excellent	Not reported	No	0.036	Photon-to-current conversion	<i>Nature Photon.</i> 2017 , 11, 315.
MAPbI ₃ microcrystal	Semiconductor	Excellent	Not reported	No	48	-	<i>Nature Photon.</i> 2017 , 11, 436.
Cs ₂ AgBiBr ₆ single crystal	Semiconductor	Excellent	Not reported	No	0.0597	-	<i>Nature Photon.</i> 2017 , 11, 726.
MAPbI ₃ polycrystalline	Semiconductor	Excellent	Not reported	No	-	Photon-to-current conversion	<i>Nature</i> 2017 , 550, 87.
MAPbBr ₃ nanocrystals	Scintillator	-	Yes	-	-	Photon-to-photon conversion	<i>This work</i> ^b

Data are from this work and from refs ^{12–16,18}. MA, CH₃NH₃.

^aWe note that scintillators are a special class of luminescence materials that have been most widely used for radiation detection by converting high-energy X-ray photons into visible light—a sensing process that is different in semiconductor materials, where the dominant process is photon-to-current conversion. The as-developed perovskite nanocrystal scintillators are solution-processable and can respond to X-rays with multicolour output, which can be readily recorded by a common digital camera.

^bWe note that the organic–inorganic hybrid QDs are less photostable than their purely inorganic counterparts and their synthesis is relatively difficult to scale up owing to the need for stringent control over the reaction conditions.